Science of the Total Environment 773 (2021) 145631

Contents lists available at ScienceDirect

Science of the Total Environment

journal homepage: www.elsevier.com/locate/scitotenv

Lignite, thermally-modified and Ca/Mg-modified lignite for phosphate remediation

Hasara Samaraweera [a], Abigail Sharp [b], John Edwards [a], Charles U. Pittman Jr [a], Xuefeng Zhang [c], El Barbary Hassan [c], Rooban Venkatesh K.G. Thirumalai [d], Sita Warren [b], Claudia Reid [a], Todd Mlsna [a,*]

[a] Department of Chemistry, Mississippi State University, Mississippi State, MS, USA
[b] Department of Engineering Management and Systems Engineering, The George Washington University, Washington, DC, USA
[c] Department of Sustainable Bioproducts, Mississippi State University, Starkville, MS 39762, USA
[d] Institute for Imaging & Analytical Technologies, Mississippi State University, Starkville, MS 39762, USA

HIGHLIGHTS

- Washed CTL phosphate uptake was 6 and 14 times greater than TL and RL.
- XRD proved $CaCO_3$, MgO, $Ca(OH)_2$, and $Mg(OH)_2$ exist on CTL.
- Unwashed CTL removed 5.2 times more phosphate than washed CTL.
- Insoluble Ca^{2+}/Mg^{2+} phosphate precipitation dominates in CTL's P uptake.
- $Mg_3(PO_4)_2$, $MgHPO_4$, $Ca_3(PO_4)_2$, and $CaHPO_4$ on P-laden CTL are slowly released to soil.

GRAPHICAL ABSTRACT

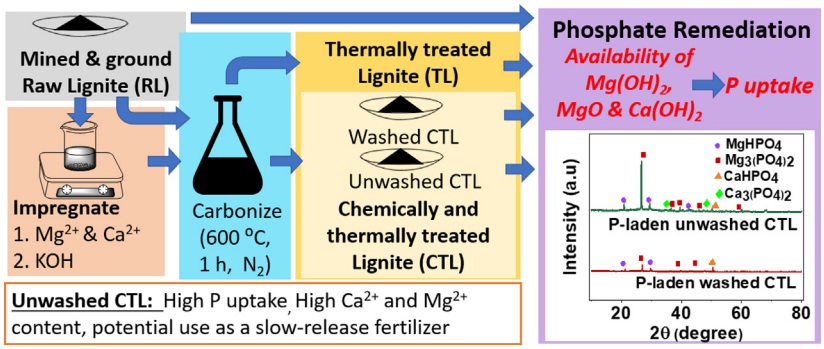

ARTICLE INFO

Article history:
Received 16 December 2020
Received in revised form 30 January 2021
Accepted 31 January 2021
Available online 5 February 2021

Editor: Jay Gan

Keywords:
Lignite
Phosphate
Adsorption
Desorption kinetics
Wastewater treatment
Surface precipitation

ABSTRACT

Aqueous phosphate uptake is needed to reduce global eutrophication. Negatively charged adsorbent surfaces usually give poor phosphate sorption. Chemically- and thermally-modified lignite (CTL) was prepared by impregnating low-cost lignite (RL) with Ca^{2+} and Mg^{2+} cations, basified with KOH (pH ~ 13.9), followed by a 1 h 600 °C pyrolysis under nitrogen. CTL has a positive surface (PZC = 13) due to basic surface Ca and Mg compounds, facilitating the aqueous phosphate uptake. $CaCO_3$, MgO, $Ca(OH)_2$, and $Mg(OH)_2$ surface phases with 0.22 μm particle sizes were verified by XRD, XPS, SEM, TEM, and EDX before and after phosphate uptake. Higher amounts of these mineral phases promoted more CTL phosphate uptake than raw lignite (RL) and thermally treated lignite (TL) without Ca/Mg modification. Phosphorous uptake by Ca^{2+}/Mg^{2+} occurs not by classic adsorption but by stochiometric precipitation of $Mg_3(PO_4)_2$, $MgHPO_4$, $Ca_3(PO_4)_2$, and $CaHPO_4$. This offers the potential of substantial uptake capacities. CTL's phosphate removal is pH-dependent; the optimum pH was 2.2. Water-washed CTL exhibited a maximum Langmuir phosphate uptake capacity of 15.5 mg/g at pH 7, 6 and 14 times higher than that of TL and RL, respectively (particle size <150 μm, adsorbent dose 50 mg, 25 mL of 25–1000 ppm phosphate concentration, 24 h, 25 °C). The unwashed CTL exhibited a maximum Langmuir phosphate removal capacity (80.6 mg/g), 5.2-times greater than the washed CTL (15.5 mg/g). Insoluble Ca^{2+} and Mg^{2+} phosphates/hydrophosphate particles dominated CTL's phosphate removal. Phosphates were recovered from both exhausted unwashed and washed CTL better in HCl than in NaOH. P-laden washed CTL exhibited a

* Corresponding author.
E-mail address: TMlsna@chemistry.msstate.edu (T. Mlsna).

https://doi.org/10.1016/j.scitotenv.2021.145631
0048-9697/Published by Elsevier B.V.

slow phosphate leaching rate under initial pH of 6.5–7.5 (52–57% over 20 days) after phosphate uptake, indicating it could serve as a slow-release fertilizer. Unwashed CTL retained more phosphates than washed CTL (cumulative q_e for 4 cycles = 391.8 mg/g vs 374.7 mg/g) and potentially improves soil fertility more.

Published by Elsevier B.V.

1. Introduction

Eutrophication, resulting from the nutrient enrichment of waters, is a current global crisis (Nixon, 2012). Phosphorous, a limiting plant nutrient widely applied in agriculture worldwide, often contaminates stormwater run-off. Environmental aqueous phosphate in concentrations as low as 100 μg/L can stimulate undesirable algal and plant blooms (Carvalho et al., 2013). These blooms lead to water quality deterioration, dissolved oxygen deficiency, biodiversity abatement, and economic losses (Zanchett and Oliveira-Filho, 2013). Annually, the US spends $2.2 billion to combat freshwater eutrophication (Dodds et al., 2009). Phosphorus regulation is essential to mitigate eutrophication. The WHO and EPA recommend that phosphorus levels should be lower than 10 mg/L in natural waters (US EPA, 2015), while phosphate concentrations should be below 0.10 mg/L in rivers and streams and below 0.05 mg/L in lakes and reservoirs, according to the Australian water quality guidelines (Huang et al., 2017). Phosphate recycling and recovery will eventually be necessary for problematic phosphorus depletion.

Phosphorous is discharged into surface waters from point source wastewater and nonpoint source run-off. Typically, municipal wastewater has approximately 5–20 mg/L total phosphorus (organic and inorganic) concentration before treatment (Hasson et al., 2016). Inorganic phosphorus mainly exists as PO_4^{3-}, HPO_4^{2-}, and $H_2PO_4^-$, depending on the solution pH (Yin et al., 2017). Traditional precipitation, reduction, flotation, coagulation, flocculation, and membrane filtration methods have many drawbacks, including initial investment, chemical consumption, efficiency, simplicity, and scalability (Langer et al., 2017; Leo et al., 2011). Efficient, practical, green, and restorable techniques have been developed for contaminant removal (Bombuwala Dewage et al., 2018; Navarathna et al., 2020). After adsorptive recovery, adsorbed phosphates have been reused as soil fertilizers, making sorption technology more ecofriendly (Mosa et al., 2020). Phosphate recovery from wastewater treatment plants (WWTP) can theoretically replace 40–50% of total phosphate application needs (Egle et al., 2016).

Coal seams are abundant, and various grades of coal can be employed as a support/sorbent to remove contaminants from aqueous solutions (Simate et al., 2016). Aqueous Cu^{2+}, Pb^{2+}, and Ni^{2+} ions were fixed by surface carboxyl and hydroxyl groups (~60–90%) on the low-rank coal, "lignite," because of its elevated cation exchange capacity and surface complexation ability (Pehlivan and Arslan, 2007). However, these oxygenated active centers have low affinities for anionic pollutants (Qi et al., 2011; Zhang et al., 2010). Introduction of Al^{3+}, Ca^{2+}, Bi^{3+}, Fe^{3+}, and Mg^{2+} to cation-deficient adsorbent surfaces previously raised phosphate removal (Fang et al., 2020; Karunanayake et al., 2019; Yang et al., 2018; Zhang et al., 2013; Zhou et al., 2013).

Yao et al., 2013 found that spent Mg-enriched tomato leaf char sorbents were successfully reused even after 10 sorption cycles and employed to treat phosphorus deficiency in soils. Equal amounts of weakly-bound P (~3.2% of the amount of PO_4^{3-} on this char) were released to water each day (average/day) over 11 consecutive days. Therefore, it behaved as a slow-release fertilizer (Yao et al., 2013). These modified, environmentally friendly sorbents could sequester C in soils and are more beneficial than commercial adsorbents. Colloidal and nano-sized MgO and $Mg(OH)_2$ surface particles on anaerobically digested sugar beet biochar improved mononuclear and polynuclear phosphate adsorption (Yao et al., 2011; Zhang et al., 2012). MgO-modified peanut shell biochar adsorbed 20% more PO_4^{3-} than raw peanut shell biochar due to the presence of MgO active surface sites. The application of P-laden MgO-biochar to coastal alkaline soils improved the available P and P uptake by field rice plants, which increased rice yields (Wu et al., 2019). Ca^{2+} was released from alkaline Ca-doped biochar ($Ca(OH)_2$: biosolids, 20 wt%) at pH = 4, into a solution where it reacts with phosphate to form insoluble brushite ($CaHPO_4$), which precipitated (Antunes et al., 2018). The maximum phosphate removal capacity of this biochar was 79 mg-P/g (at initial pH 3). Elevated phosphate sorption was achieved by a novel $Mg(OH)_2/ZrO_2$ composite (MZ) resulting from both 1) ligand exchange between the ZrO_2 and $MgHPO_4$ and 2) reaction between $Mg(OH)_2$ and phosphate forming $MgHPO_4$ and $Mg_3(PO_4)_2$ (Lin et al., 2019). Dissolved Mg^{2+} originating from the $Mg(OH)_2$ also synergistically enhanced the phosphate-binding on the ZrO_2 component in MZ. Ca^{2+}-Mg^{2+} pre-loaded (19 wt% Mg^{2+} and 19 wt% Ca^{2+}/biomass) on corncob biochar had a very high (326 mg/g) Langmuir phosphate uptake capacity (Fang et al., 2015). No previous work has been published regarding the Ca^{2+}/Mg^{2+} modification of cheaper and widely available lignite to remove aqueous phosphates.

In this study, we converted locally abundant raw lignite (RL) into a chemically- and thermally-modified lignite (CTL) via surface deposition of $MgO/Mg(OH)_2$ and $CaO/Ca(OH)_2$ and pyrolysis at 600 °C. CTL promoted phosphate removal due to the formation of precipitates ($Mg_3(PO_4)_2$, $MgHPO_4$, $Ca_3(PO_4)_2$, and $CaHPO_4$) formed upon reaction of solution phosphate with Mg^{2+} and Ca^{2+} ions released from CTL. Crystallographic phase structures on pre- and post-P-sorbed materials were characterized by XRD. The particle elemental compositions were further characterized by XPS/EDX analysis. CTL phosphate sorption follows the pseudo-second-order kinetic model. Untreated RL showed significantly higher P specific sorption per unit surface area (12.1 mg/m^2) than TL (0.4 mg/m^2) and washed CTL (1.2 mg/m^2) (40 °C, pH 2.2, particle size, particle size <150 μm).

2. Materials and methods

Lignite was provided by the Mississippi Lignite Mining Company (Red Hills Mine, Ackerman, MS, USA). Raw lignite (RL) was washed thoroughly with deionized water to remove extraneous materials such as dirt, sand, and other impurities, followed by oven drying at 80 °C for 48 h (1 atm, air). The dried lignite was ground into fine particles using a high-speed multifunctional grinder (CGOLDENWALL, China, 2500 W, 36000/min, model no: HC150T2) and sieved to 150–300 μm. A high SiO_2 fraction was (19.9%) in this lignite's ash (total ~ 25.0%). All chemicals used, including magnesium sulfate, calcium sulfate hemihydrate, potassium hydroxide, concentrated sulfuric acid, ammonium molybdate, and ascorbic acid, were analytical grade and purchased from Sigma Aldrich.

2.1. Preparation of Ca^{2+} and Mg^{2+}-loaded lignite adsorbent (CTL)

RL (100 g), washed and dried as previously described, was impregnated with a single solution of $MgSO_4$ and $CaSO_4$ formed by combining two solutions prepared separately. A 10% aqueous $MgSO_4$ solution (10 g of $MgSO_4$ [0.083 mol] dissolved in 100 mL of water, [1.992 g of Mg]) was prepared. Then a 10% aqueous solution of $CaSO_4 \cdot 1/2H_2O$ (10 g of $CaSO_4 \cdot 1/2H_2O$ [0.069 mol] dissolved in 100 mL of water, [2.76 g of Ca]) was made and added into the $MgSO_4$ solution. Next, 1.5 M aqueous KOH (350 mL, 29.4 g of KOH, 13.9% wt. of K) was added to the combined $MgSO_4$ and $CaSO_4 \cdot 1/2H_2O$ solution to adjust the pH to ~13.9. RL (100 g) was stirred in the Ca^{2+}-Mg^{2+} and KOH containing solution for 1 h and aged 24 h. Then, the resulting slurry was transferred into watch glasses.

These slurries were then oven-dried (1 atm, 105 °C, 4 h) and vacuum oven-dried (0–4.9 atm, 60 °C for overnight). The dried material weighs 139.2 g. This was then pyrolyzed at 600 °C in a muffle furnace under nitrogen at a 20 °C/min ramp rate to 600 °C, followed by holding at 600 °C 1 h. This temperature was chosen according to Takaya et al., 2016. The resulting solid (wt. 89.0 g) was washed with DI water, oven-dried (1 atm, 80 °C overnight), giving a solid (wt., 53.9 g). This difference showed that substantial amounts (35.1 g) of soluble Ca^{2+}, Mg^{2+}, and K^{+} compounds were removed. This resulting CTL was crushed to particle sizes smaller than 0.3 mm. CTL (chemically- and thermally-treated lignite) was sieved into three particle sizes (<150, 150–300, and > 300 μm) and stored in air-sealed containers for future characterization and adsorption experiments. An as-received raw lignite sample (100 g) was identically pyrolyzed at 600 °C, without adding any chemicals, generating thermally-treated lignite (TL) (59.5 g) to compare with CTL and RL, after a wt. loss of 40.5 g.

2.2. Characterization techniques

Detailed characterization methods can be found in the supplementary materials. Surface areas, DFT pore sizes, pore volumes, and micropore volumes of RL, TL, and CTL were determined. The surface areas were measured using N_2 and CO_2 physisorption using the BET method run on a Micromeritics Tristar II Plus surface analyzer. Scanning electron microscopy (SEM) was performed on adsorbents using a Carl Zeiss EVO50VP Variable Pressure Scanning Electron Microscope with an accelerating 15 kV voltage. A JEOL 2100 200KV TEM with Oxford X-max 80 EDS detector was used to evaluate the CTL's inner morphology. Surface region (depth of 3.1 μm) elemental distribution was determined by Energy-dispersive X-ray spectroscopy using a Bruker Quantax 200 X Flash EDX Spectrometer System (LN2-free high-speed 30mm^2 SDD Detector) under a magnification 150×, employing an interaction diameter of ~3.8 μm. Surface chemistry was studied using X-ray photoelectron spectroscopy to elucidate elements present and their oxidation states to a maximum detection depth of 80 Å. XRD analysis was performed on RL, TL, and CTL to a penetration depth of 0.5 mm and a spot size of 1 cm^2. An ECS 4010 elemental combustion system (Costect Analytical Technologies Inc.) was used to analyze the C, H, and N composition. The samples were oven-dried for 2 h at 105 °C before assessing their moisture contents. The samples were heated in air in a muffle furnace at 750 °C for 4 h in an uncovered porcelain dish to determine their ash contents. Organic oxygen percentage was calculated by (100 - [C + H + N + ash]). NaCl solutions, adjusted from pH 2–12 using 1 M HNO_3 and 1 M NaOH, were used with a pH meter to determine the adsorbents' point of zero charges (PZC). Total Mg and Ca loadings of CTL were determined using AAS after complete acid digestion with 1:1 95% H_2SO_4/70% HNO_3 (50 mL).

2.3. Adsorption experiments

Unless otherwise specified, a 0.05 g adsorbent dose, 50 ppm phosphate concentration, and 25 mL solution volume were used in batch experiments without a pH adjustment (pH = 5.5). This initial pH changed due to leaching of Ca^{2+}/Mg^{2+} from the CTL, as presented in Section 3.4.2. Batch experiments were conducted in a Thermo Forma Orbital Shaker (200 rpm, 25 ± 0.5 °C) for 24 h to achieve equilibrium. The vials were removed after the shaking period, and the suspensions were filtered through Whatman 1001–110 Qualitative filter papers (11.0 cm diameter, pore size, 11 μm). Three replicates of each experiment were performed. Solution pH was determined before and after adsorption. The residual phosphate concentrations in the filtrates were determined calorimetrically by following the reduction of the blue-colored molybdenum phosphate complex at 830 nm using a Shimadzu, UV-2550 double beam Spectrophotometer. The analysis was conducted according to the ascorbic acid method (Lozano-Calero et al., 1996). The detailed phosphate determination procedure is described in the supplementary materials (Section 1.3.1).

Phosphate sorption versus pH was determined by varying the solution pH from 2.2 to 11.5 by dropwise addition of 1 M HCl or 1 M NaOH. Kinetic experiments employed samples containing 50 ppm phosphate concentrations, collected at preselected times (5 min. up to 24 h). Adsorption isotherm experiments were conducted using 25–1000 ppm phosphate solutions under the optimum adsorption pH (~2.2) and practically important pH level (pH ~ 7) at 25, 30, and 40 ± 0.5 °C for 24 h. Data evaluation methods (including isotherm and kinetic model fittings) and equations were shown in supplementary materials (Section 2.2).

2.4. Ca and Mg leaching from CTL

A control experiment was conducted to investigate Ca^{2+} and Mg^{2+} leaching into DI water at pH 2.2. Washed CTL (0.1 g) was added into 50 mL DI water (without phosphates) at pH 2.2. This suspension was stirred for 24 h, at 25 °C (200 rpm), filtered, and the filtrates were quantified using AAS for leached Ca and Mg amounts.

2.5. CTL regeneration, reuse, and desorption kinetics

The regeneration tests for P-laden washed CTL and P-laden unwashed CTL were conducted using an aqueous NaOH stripper and performed according to Du et al., 2019 with a minor modification. CTL (1.5 g) was first equilibrated with 750 mL of 1000 ppm phosphate solution in a mechanical shaker (200 rpm, 25 °C, 24 h) at pH 7. After phosphate uptake, the suspension was filtered, and the P-loaded CTL was washed with DI water (~50 mL) to remove traces of unadsorbed P and only H-bonded phosphate on the CTL surface. After oven-drying (1 atm, 2 h, 105 °C), P-loaded CTL was desorbed using a 1 M NaOH (10 mL, 25 °C) stripping treatment while stirring in a single batch. The filtrates were analyzed for released phosphate concentrations using the same colorimetric technique as previously described. Four adsorption-desorption cycles were performed. Since NaOH was not a potent phosphate stripping agent (as explained further in Section 3.5), both washed CTL and unwashed CTL sorbents were subjected to acidic stripping (Fig. 5c, d). Initially, a 1000 ppm phosphate solution (750 mL for both) was used to load P onto 1.5 g of each adsorbent at pH 7. Desorption was performed using 0.5 M HCl (10 mL) as the stripping agent.

A desorption kinetic study was conducted on P-laden washed CTL. Initially, phosphate was adsorbed onto CTL (0.6 g) from a solution (100 ppm, 300 mL) in a plastic bottle during vigorous shaking for 24 h (pH 7, 25 °C, 200 rpm). This suspension was filtered; the P-loaded CTL was washed with DI water (~150 mL) to remove unadsorbed P and then oven-dried (1 atm, 105 °C) overnight. A series of 100 mL DI water samples (pH = 6.5, 7.0, and 7.5) were prepared, and P-loaded CTL (0.15 g) was added to each. Samples (1 mL aliquots) were removed on consecutive days, and leached phosphate concentrations were determined as described in Section 2.3. The pH of the DI water was also measured each day.

3. Results and discussion

3.1. Composition and textural properties of RL, TL, and CTL

Coal surface area per unit weight depends on its source and rank and are typically ˷ 100 m^2/g for lignite (Mohan and Pittman Jr., 2006). A very low lignite surface area (S_{BET}, 1 m^2/g) was also reported (Milicevic et al., 2012). Specific surface areas for RL, TL, and CTL were calculated through Brunauer–Emmett–Teller (BET) theory and shown in Table 1. CO_2 and N_2 were employed as adsorbates for the BET surface area determinations. BET using N_2 can be inaccurate for samples with higher micropore contents (<1.2 nm) because the slow rate of N_2 diffusion blocks pore filling at 77 K (de Jonge and Mittelmeijer-Hazeleger, 1996). In contrast, CO_2 fills micropores far faster because of its far higher thermal energy at

Table 1
Textural and elemental properties of RL, TL, and CTL (washed form).

Parameter	Adsorbent		
	RL	TL	CTL (washed form)
BET (m^2/g)[a] at the particle size 150–300 μm			
N_2	0.4	46.0	21.0
CO_2	35	127	120
q_e (mg/g)[b] at 25 °C	2.4	0.6	11.6
Sorption ability (mg/m^2) (N_2 BET) [c]	6.0	0.01	0.6
Sorption ability (mg/m^2) (CO_2 BET)	0.07	0.05	0.10
Pore volume (cm^3/g)			
N_2	0.0008	0.0109	0.0054
CO_2	0.0077	0.0270	0.0184
Micropore volume (cm^3/g)			
N_2	0.0003	0.0100	0.0031
CO_2[d]	N/A	N/A	N/A
DFT pore size (nm)[e]			
N_2	2.9	2.3	1.7
CO_2	0.54	0.50	0.49
Moisture (%)	3.2	3.2	2.5
C (%)	39.4	26.5	13.5
H (%)	2.7	1.4	0.8
N (%)	1.2	1.4	0.9
O[f] (%)	16.7	11.7	9.8
Ash (%)	25.0	59.0	75.0
PZC	3.9	9.4	11.8
Yield (%)	–	59.5	38.7

[a] Adsorbent surface areas were measured at the particle size 150–300 μm. When the particle size of all three adsorbents decreased to <150 μm, their BET surface areas (using N_2) increased (RL = 2.9 m^2/g, TL = 120 m^2/g, CTL = 60 m^2/g).
[b] RL, TL, and CTL uptake capacities (q_e) at the particle size 150–300 μm were obtained from Fig. S4a.
[c] Phosphate removal capacity was divided by the absorbent surface area to obtain specific sorption ability (mg/m^2).
[d] Micropore volumes using CO_2 were negligible for all three adsorbents.
[e] DFT theory accurately describes the pores in micro- and mesopore range.
[f] O content presented here does not reflect the oxygen associated with their inorganic constituents.

0 °C (McLaughlin, 2012). Specifically, the BET surface areas using N_2 were 2.9, 46, and 21 m^2/g (Table 1) for RL, TL, and CTL, respectively (particle size, 150–300 μm) (Table 1). The corresponding surface areas using CO_2 were significantly larger (35, 127, and 120 m^2/g for RL, TL, and CTL, respectively), indicating the abundance of narrow micropores in these samples.

RL's low surface area (35 m^2/g) increased to 127 m^2/g in TL after heating at 600 °C under N_2. When the lignite is pyrolyzed, the moisture and volatile and decomposing matter are evaporated. This out-gassing leads to new pore formation, or opening of closed pores, creating higher surface area materials. The average pore volume increased, and the average pore radius decreased slightly in TL vs. RL (Table 1). A 40.5% weight loss occurred after RL's thermal treatment at 600 °C (yield of TL was 59.5%). The CTL surface area tripled versus RL (120 vs. 35 m^2/g) due to fine $MgO/Mg(OH)_2$, $CaO/Ca(OH)_2$, and $CaCO_3$ particle formation, possibly loss of tightly held water and lignite structural changes. The oxides form the corresponding hydroxides on water washing. These surface deposits close some CTL pores, reducing total pore volume relative to TL. Mg/Ca compound existence on the CTL surface was observed from SEM/EDX observations (Fig. 2d-i), which increase the removal of phosphate. CTL's surface area, measured using CO_2, is slightly lower than TL (Table 1), which is consistent with the previous literature. The incorporation of $MgCl_2$ into wood biomass caused the micropores' blockage (MgO precipitation) and reduced the surface area by over one-third (Chen et al., 2020).

Coals contain micropores (<1.2 nm), mesopores (1.2–30 nm), and macropores (>30 nm) (Simate et al., 2016). Pore sizes obtained from the NL-DFT method were presented in Table 1. DFT theory accurately describes the pores in the micro- and mesopore range. NL-DFT treats the sample as an effective porous material, where heterogeneity is approximated by a distribution of pore sizes. Thus, heterogeneity due to the chemical groups on the surface, pore shape variations, pore networking, and blocking effects is not accounted for explicitly (Fraissard and Conner, 1997; Inagaki, 2006). Pore size distributions of RL, TL, and CTL were obtained using both N_2-DFT (Fig. S1a-c) and CO_2-DFT (Fig. S1d-f). RL has a wide pore size distribution (2–25 nm), as illustrated in Fig. S1a. TL has a higher mesopore fraction than RL, distributed from 1.8 to 2.3 nm by N_2-DFT (Fig. S1b). CTL is highly microporous, with pores narrowly distributed around 1.8 nm (Fig. S1c). CO_2-DFT found average pore diameters ranging from 0.49 to 0.54 nm for these three lignite adsorbents (Fig. S1d-f and Table 1). Phosphate anions have diameters of 0.223 nm, which increase to 0.339 nm with its water hydration shell (Zhong et al., 2015). Thus, a portion of micropores in all three adsorbents have access to hydrated phosphate.

The PZC of TL (~9.4) versus RL (~3.9) (Table 1) reflects the presence of basic oxides, hydroxides, and carbonates formed during the 600 °C lignite pyrolysis. The high TL porosity was caused by mass loss. The following extensive washings removed many basic oxides, hydroxides, and some carbonates from TL. The PZC of CTL increased to 11.8. The abundant silica was detected in both CTL and TL is from original lignite ash (19.9%, SiO_2), which is in good agreement with XRD analysis. Lignites are carbonaceous with 20–25% fixed carbon (Bowen and Irwin, 2008). RL contains 39.4% C (Table 1). Heat treatment of RL reduced the C percentages remaining in TL (26.5%) (Table 1) while increasing the Al (0.3% to 2.3%) and Si (9.3% to 35.7%) contents in TL vs. RL (Table S1, Figs. S2–S3). Organic matter gasification during thermolysis reduced carbon levels (Cao and Harris, 2010). The ash content of washed CTL (SiO_2, 54.4%, Al_2O_3, 12.1%, $CaCO_3$, 3.75%, and MgO, 4.8%) totals 75.0% (Table 1), is consistent with the ash content (~74.6%) determined by TGA analysis run at 0–1000 °C under O_2 (heating rate 10 °C/min) (Fig. 1a).

After complete acid digestion of washed CTL, Mg (2.9%) and Ca (1.5%) weight percentages were determined using AAS (Table S1). Bulk Ca and Mg percentages were smaller than the amounts detected using SEM/EDX studies (Mg = 2.8% vs. Ca = 5.9%), and the percentages quantified using XPS (Mg = 12.4% and Ca = 4.8%) (more information in Sections 3.3 and 3.4). Thus, Ca and Mg species are more concentrated on the top ~8 nm of the CTL sample. After washing and drying, RL (1 atm, several days, 80 °C) and TL moisture contents were similar (~3.2%) (Table 1). The inherent moisture of coal can be either the moisture within the micropores and microcapillaries while deposited in the ground (interior adsorbed water) or surface-bound water (Karthikeyan et al., 2009). CTL has a lower moisture content (~2.5%) than TL and RL (~3.2% in both) after heating the samples for 2 h in a hot air-oven at 105 °C.

3.2. XRD analysis

The high background intensity in the RL XRD spectrum indicates an extensive amorphous carbon nature (Fig. 1b). The crystalline peaks at 2Θ = 24.9° (002) and 38.4° (100) depict the coal samples' aromatic stacking in some graphitic like carbon structures. The (002) peak's asymmetric nature is due to the association of a γ peak from aliphatic side chains attached to the aromatic carbon (Zhao et al., 2020). CTL's XRD spectrum has many crystallite phases, in which the peaks are sharp, complicated, and highly ordered compared to RL (Fig. 1b). Specifically, sharp peaks located at 2Θ = 20.8° ("Quartz R100134 - RRUFF Database,", 2020) and 26.6° correspond to the (100) and (011) reflection of quartz (SiO_2). Amorphous SiO_2 existed in RL, but after thermal treatment at 600 °C for 1 h in the presence of Ca and Mg salts, sintering produces larger SiO_2 crystallites. These exhibit high-intensity peaks in XRD patterns (Buscarino et al., 2011). The intense peak at 2Θ = 29.4° is due to the $CaCO_3$ formed in the CTL, with an average $CaCO_3$ crystal size of 38.5 nm, determined by the Debye-Scherrer equation (Section 2.1, supplementary materials). This demonstrates the formation of nano-sized $CaCO_3$ grains on the CTL during the pyrolysis. $Mg(OH)_2$ and $Ca(OH)_2$ also formed and precipitated onto the CTL surface during synthesis

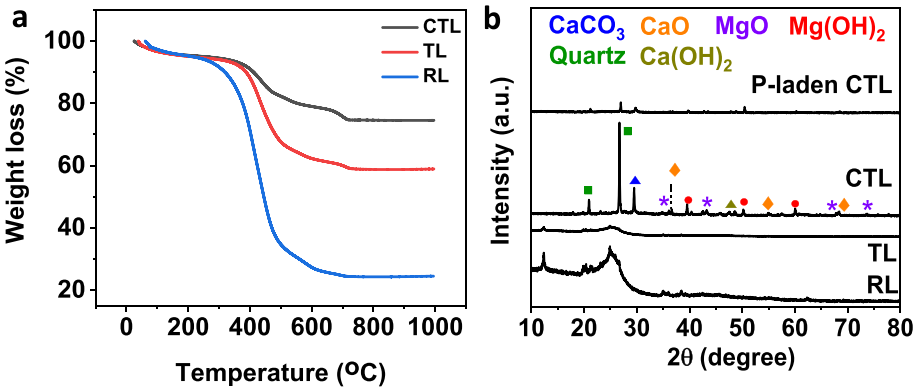

Fig. 1. a) TGA analysis of RL, TL, and washed CTL under O_2 (heating rate, 10 °C/min). b) XRD analysis of RL, TL, washed CTL, and P-laden washed CTL. Phosphates were adsorbed to the CTL surface at pH = 2.2.

when the pH rose using KOH. These hydroxides have lower solubility product constants than their sulfate precursors (Table S2). Calcite was formed due to the inert pyrolytic atmosphere, where calcium hydroxide reacts with carbon dioxide produced from char particles during the pyrolysis process. Small amounts of $Ca(OH)_2$ (2Θ = 47.6° and 50.7°) and CaO (2Θ = 37.0°, 54.0°, and 67.0°) are present on the CTL surface (Fig. 1b). CaO peaks were less intense than $Ca(OH)_2$, indicating the surface exothermic (ΔH = −104 kJ/mol) hydration of CaO to $Ca(OH)_2$ occurred (Criado et al., 2014). Residual CaO/$Ca(OH)_2$, MgO/$Mg(OH)_2$, K_2O, KOH, and K_2CO_3 on the CTL surface and encapsulated onto some pores was removed during the washing step after the pyrolysis. In this wash, the initial 89.0 g mass was reduced by 35.1 g leaving 53.9 g afterwards.

Other CTL peaks at 21.2°, 39.7°, 50.5°, and 60.0° accredited to $Mg(OH)_2$ (Zhang et al., 2015). The peaks at 2Θ = 36.6°, 43.4°, 62.6°, and 74.7° can be indexed to the 111, 200, 220, and 311 planes of face-centered cubic surface MgO. The tiny 43.3° peak indicated traces of MgO (~50.5 nm) exist on the CTL. MgO formation on the CTL is caused by the dehydration of $Mg(OH)_2$ (ΔH = +81 kJ/mol) (Mastronardo et al., 2016). If $MgSO_4$ was present, it could decompose to MgO under the reducing atmosphere (Scheidema and Taskinen, 2011).

After P removal at pH 2.2, peaks located at 2Θ = 29.8° and 39.7° ($CaCO_3$ and $Mg(OH)_2$) suffered significant intensity reduction, and the peaks centered at 60° and 36°-37° ($Mg(OH)_2$) and 47°-48° ($Ca(OH)_2$) vanished in P-laden CTL (Fig. 1b). Dissolution of $CaCO_3$, $Mg(OH)_2$, and $Ca(OH)_2$ in an acidic medium form soluble Ca^{2+}/Mg^{2+}, which reacts with phosphate anions in solution and forms corresponding insoluble phosphates and hydrophosphates in the CTL. This reduced the $CaCO_3$ and $Mg(OH)_2$ peak intensities (Fig. 1b). The new XRD peaks in P-laden CTL (Fig. 1b) were assigned to $MgHPO_4 \cdot 1.2H_2O$, $Mg_3(PO_4)_2 \cdot 8H_2O$, $CaHPO_4$ and $Ca_3(PO_4)_2$ (Binitha and Pradyumnan, 2013; Hung et al., 2012, p. 50; Zhang et al., 2016) (more information in Section 3.5). No $Ca(OH)_2$ is retained in CTL at pH = 2.2 (K_{sp} = 5.5×10^{-6}) (Table S2, supplementary materials). The hydroxyapatite ($Ca_5(PO_4)_3(OH)$) diffraction pattern was not observed in the P-laden XRD spectrum. Next, when CTL was exposed to 1000 ppm phosphate solution (pH 2.2) at 25 °C, the pH increased to ~10.0 immediately (more information in Section 3.4.2). At this pH, phosphates mainly exist as HPO_4^{2-}/PO_4^{3-} The $Ca(OH)_2$ released under acidic conditions precipitated as brushite ($CaHPO_4$). Brushite is the most thermodynamically stable phase relative to other calcium compounds at room temperature in the lower pH region. Here, Ca^{2+} reacts with $H_2PO_4^-$ producing brushite, as demonstrated by XRD (Wuthier et al., 1985). Previously, brushite was formed on P-laden Ca-doped biochar (~20 wt% $Ca(OH)_2$/biochar) at pH = 2 (Antunes et al., 2018). $CaCO_3$, the major phase retained in the CTL surface, is insoluble ($K_{sp} = 2.9 \times 10^{-9}$). However, it releases dissolved Ca^{2+} at pH 2.2, which forms a surface $CaHPO_4$ precipitate.

3.3. Adsorbent morphologies

3.3.1. SEM, SEM-EDX, and TEM analysis of adsorbents

SEM analyses examined the morphology and chemistry changes after thermal and chemical modifications to RL (Fig. 2 and Fig. S2). RL's relatively smooth surface morphology became more irregular in TL and washed CTL (Fig. 2a). TL contained many micron-sized pores (Fig. 2b, marked with arrows). Most surface particles deposited on CTL are agglomerated and roughen the surface (Fig. 2c). SEM/EDX mapping of CTL (Fig. 2d-h) displayed Mg, Ca, C, and O that are distributed in overlapped regions, in accordance with $MgCO_3$, $CaCO_3$, MgO, $Mg(OH)_2$, and $Ca(OH)_2$ present on the surface (discussed in Section 3.4 in detail). These particle size diameters were mostly below 2 μm (Fig. 2c). Chemical impregnation and subsequent thermal conversion at 600 °C deposits Ca and Mg minerals onto CTL, appearing as lightly shaded primary particles and/or aggregated clusters (Fig. 2c).

RL exhibits abundant C, O, with Al, Si, Mg, Ca, K, and Fe in the surface region (Fig. S2). SEM-EDX analysis of CTL after exposure to pH = 2.2 DI water (25 mL, 200 rpm, 24 h, 25 °C), filtering and drying showed smaller Ca, Mg, Si, K, and O atomic percentages (Fig. 2p and q) compared to before washing. Also, pH increased from pH = 2.2 to pH 9.3, and a 30% CTL weight loss occurred. Acidic rinsing dissolved many mineral oxides from the surface and caused the EDS peak reductions. The obvious loss of basic Mg and Ca compounds took place from CTL under acidic conditions. The Mg^{2+} and Ca^{2+} ions released then reacted to form insoluble phosphates, which precipitated and were observed in the P-laden CTL EDX spectrum (Fig. 2r). Ca and Mg compounds retained in unwashed CTL exhibited more phosphate removal than washed CTL (80.6 mg/g vs. 15.5 mg/g) (Section 3.4.3).

Fig. 2j-o shows the washed CTL SEM/EDX analysis after exposure to 100 ppm phosphate solution (labeled P-laden CTL). After phosphate uptake, Ca dropped from 5.9% to 1.5% and Mg dropped from 2.8% to 1.3% atomic percentages on the P-laden CTL surface. P-laden CTL EDX elemental mapping found that phosphorus was concentrated in the regions where Ca, Mg, and O had deposited (Fig. 2l-o). $Mg_3(PO_4)_2$, $MgHPO_4$, and $CaHPO_4$ were precipitated on CTL at pH 2.2 during this P uptake, according to XRD/XPS studies. This occurred because both Ca^{2+} and Mg^{2+} dissolved into water, where it reacted with HPO_4^{2-}/PO_4^{3-}. Previous studies found that phosphate uptake also occurs by surface deposition (Yao et al., 2011). The EDX electron spectrum found 3.5 wt% P in P-laden CTL (Fig. 2r). This contrasts sharply with P-laden RL (0.8 wt% P) and P-laden TL (1.3 wt % P) (data is not presented). The CTL vs RL wt% of Mg (2.8% vs 0%) and Ca (5.9% vs. 0.02%) (Table S1) favor phosphate uptake by CTL. This confirms the combined chemical and thermal modification process using Mg and Ca enhances lignite's use for phosphate remediation.

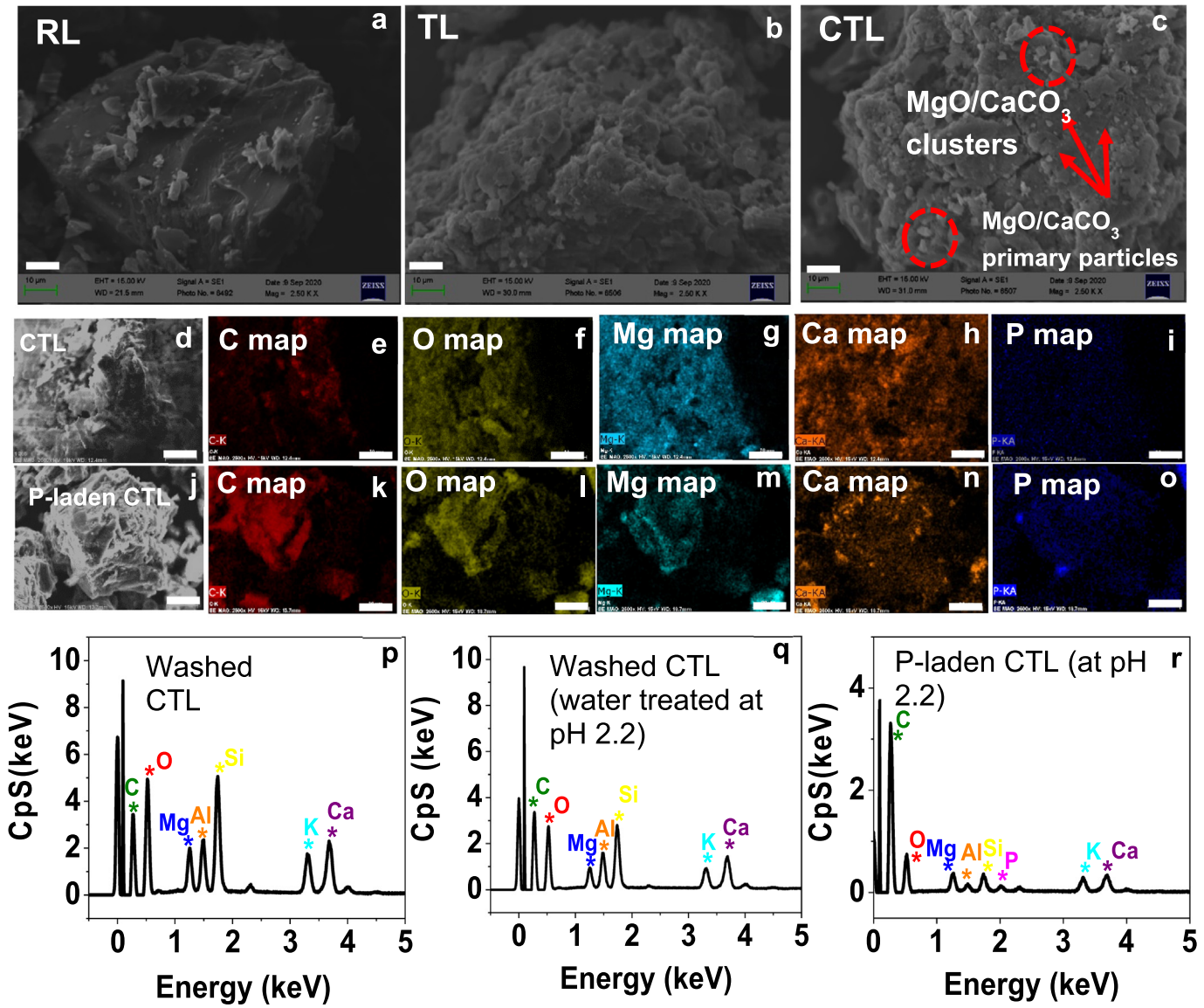

Fig. 2. (a-c) SEM images of RL, TL, and washed CTL (15 kV, scale bar 20 μm, resolution 2.50 kX); brightly colored areas covered with red circles in (c) indicate the surfaces of Mg and Ca hydroxide/oxide/carbonates of washed CTL. SEM-EDX mapping of washed CTL before (d-i) and after (j-o) P uptake (scale bar 20 μm, resolution 2.5 kX). P-laden washed CTL (j-o) confirms phosphates were adsorbed onto the surface Mg oxides/carbonates of CTL (scale bar 20 μm, resolution 2.5 kX). P-loaded washed CTL was prepared at pH 7, with 100 mg/L phosphate (25 mL) equilibrated with 50 mg of CTL for 1 h at 25 °C (2 g/L dose). SEM/EDX electron spectra for washed CTL (p), washed CTL (2 g/L) was exposed to water at pH = 2.2 (q), and 1000 mg/L phosphate (25 mL) at pH = 2.2 (r), depicting the surface regions elemental composition.

Nevertheless, RL can be used alone without expending any process modification costs to adsorb phosphate.

TEM images of CTL showed MgO clusters (black) dispersed on the char matrix (grey) (Fig. 3a). The flake-like morphology of MgO at a higher resolution (Fig. 3b) displayed tiny MgO crystallites (size 20–30 nm) aggregated to larger MgO cluster sizes between 200 nm to 2 μm. The dark field image of CTL showed the MgO clusters (white) in a dark background (char matrix). These MgO clusters were confirmed by acquiring the sample's SAED pattern (Fig. 3d), with a d spacing of 0.211 nm. This d spacing belonged to MgO-002 crystal phase according to the crystal structure database. CaO hydration is an exothermic ($\Delta H = -104$ kJ/mol) and a spontaneous process (Criado et al., 2014). However, precipitated $Ca(OH)_2$ has a high solubility product (Table S2), and it is hard to observe on CTL after washing. Low hydration of MgO was reported ($\Delta H = +81$ kJ/mol) (Dung and Unluer, 2017; Mastronardo et al., 2016), making it comparatively more stable than CaO on the CTL.

3.4. Adsorption performance

3.4.1. Effects of low initial phosphate concentration, adsorbent particle size and adsorption kinetics

Efficient sorbents have a high adsorbate affinity at low adsorbate concentrations (Wu et al., 2020). Sorption affinities of RL, TL, washed CTL, and unwashed CTL were tested at low phosphate concentration (0.4 ppm) (Fig. 3e). The unwashed CTL afforded more than 98% of phosphate removal versus RL (8%), TL (38%), and washed CTL (86%), making it a promising selective phosphate adsorbent. Unwashed CTL achieved ultra-low equilibrium phosphate concentration (0.006 ppm) at an initial phosphate conc. of 0.4 ppm. This value is below USEPA's suggested phosphate level in water, 0.01 ppm to prevent possibility of eutrophication (US EPA, 2018).

When the particle size decreased from >300 to <150 μm, phosphate adsorption increased by 37% (RL), 80% (TL), and 33% (CTL) (Fig. S4a) (Adsorbent dose 50 mg, 25 mL of 50 ppm [phosphate], 24 h, pH 5.5,

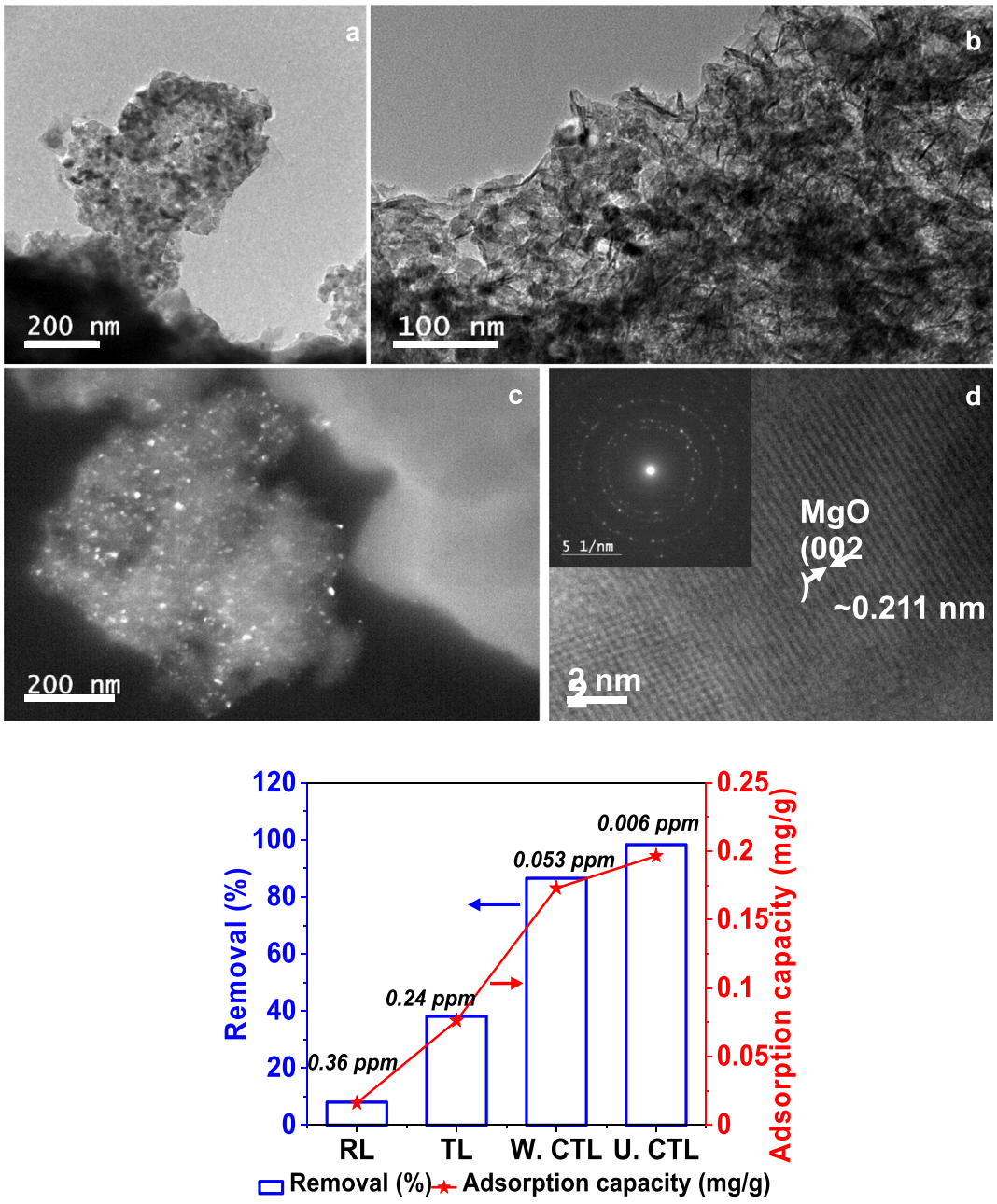

Fig. 3. a) Bright-field TEM image of washed CTL representing MgO (002) clusters (black) dispersed on char matrix (grey), b) flake-like morphology of washed CTL was visible at high magnification, c) dark-field TEM imaging of washed CTL; white spots are MgO particles dispersed on char matrix d) high-resolution TEM image of a MgO particle showing overlapped lattice fringes (inset showed the SAED pattern of that MgO particle). e) Phosphate uptake from the low initial phosphate concentration (0.4 ppm, 25 mL) on (0.05 g doses) RL, TL, washed CTL (W. CTL), and unwashed CTL (U. CTL) at 25 °C for 24 h. Equilibrium phosphate concentrations after uptake are presented on the top of the blue bars.

25 °C). The <150 μm particle size had a higher phosphate removal and was selected for adsorption isotherm experiments. Interestingly, RL surfaces have a higher specific sorption ability per unit surface area (6.0 mg/m^2) than CTL (0.6 mg/m^2) and TL (0.01 mg/m^2) (adsorbent dose 50 mg, 25 mL of 50 ppm [phosphate], 24 h, pH 2.2, 25 °C, particle size, 150–300 μm) (Table 1). When RL was ground to smaller particle size, <150 μm RL's sorption ability was lower (1.0 mg/m^2). This is due to the increase of its surface area (2.9 m^2/g) at the size <150 μm. RL can be used for water treatment with lower production costs than CTL, as it requires no pre-treatment, and is plentiful and cheap. CTL's higher capacity (11.6 mg/g) (Table 1) is due to the dissolution of Ca^{2+} and Mg^{2+} ions, which precipitates its phosphate and hydrophosphate salts.

The CTL P uptake initially increased rapidly (Fig. S4b), and > 80% of the maximum adsorption capacity (17.9 mg/g) was adsorbed within 5 h (adsorbent dose 50 mg, 25 mL solution volume, 50 ppm phosphate concentration, 25 °C). This rise was due to the presence of un-occupied adsorption sites on the CTL surface at the beginning. However, CTL P removal equilibrium was achieved after ~20 h, similar to phosphate adsorption into MgO-digested sugar beet tailings biochar (Yao et al., 2011) and Mg-enriched tomato tissue biochar (Yao et al., 2013). Rapid initial and slow subsequent uptake suggest that precipitation is not the only removal path. The reported abundant nano-CaO and MgO (PZC > 10) surface species and a very high BET specific surface area of Ca-Mg/biochar (487.5 m^2/g) accelerated the P binding equilibrium to within 30 min. (Fang et al., 2015). The slow P removal kinetics by washed CTL can be due to the much smaller quantities of MgO and -$Mg(OH)_2$ (after washing), which reduces the amount and rate of phosphate uptake by precipitation and adsorption. The relatively low CTL surface

area (BET—N_2, 21 m^2/g and BET- CO_2, 120 m^2/g) reduces the extent of physisorption. The best-fit parameters of each kinetic model are listed in Table S3. The calculated q_e of CTL (18.9 mg/g) is close to the experimental value (17.9 mg/g). CTL phosphate removal follows the pseudo-second-order kinetic model ($R^2 = 0.99$), suggesting chemical bond formation. Similar trends were observed in Ca-doped biochar (Antunes et al., 2018) and MgO-modified diatomite (Xie et al., 2014). Phosphate binding onto Mg-enriched tomato tissue could be better described by an n^{th} order model and followed multiple mechanisms (Yao et al., 2013).

Phosphate adsorption into TL ($k_2 = 0.3$ g/mg min) is faster than CTL ($k_2 = 0.04$ g/mg min). As the contact time increases, TL's kinetic curve exhibited a rapid phosphate uptake and plateaued ~5 h, with a maximum phosphate absorbance of 1.9 mg/g. Pseudo-second-order kinetic model describes TL phosphate removal well.

3.4.2. pH dependence of P adsorption

Phosphate sorption by RL is only weakly pH-dependent (Fig. 4a). At ~pH 2.2, phosphate sorption was highest on washed CTL (22.9%) versus TL (14.7%) and RL (1.7%) (adsorbent dose 50 mg, 25 mL of 50 ppm phosphate concentration, 24 h, particle size 150–300 μm, 25 °C). The CTL and TL (PZCs, 11.8, and 9.4) were positively charged under typical wastewater pH conditions (pH = 6–9); therefore, they can be successfully employed in phosphate removal from acidic wastewaters (mining wastewater, acidic leachates from wet chemical P-recovery process). Both CTL and TL (Table 1) demonstrated higher phosphate uptake per unit weight than RL due to their more basic PZC (Fig. 4a) and higher surface areas. Removal efficiency changes occur with surface property alterations and phosphate speciation. H_3PO_4 exhibits pKa1 = 2.12, pKa2 = 7.21 and pKa3 = 12.67 and its aqueous speciation is plotted in Fig. 4a. When the initial pH is ~2–3 (but with a highly alkaline final equilibrium pH ~ 9.4), positive sites on the CTL and TL surfaces can attract HPO_4^{2-}/PO_4^{3-} adsorption. In an earlier study, phosphate anion adsorption was favorable when the solution pH was below the PZC of a Fe–Al–Mn tri-metal oxide (~9.0) (Lǔ et al., 2013).

Leaching of Mg^{2+} and Ca^{2+} from washed CTL was investigated at pH 2.2, 7, and 10 in the presence/absence of dissolved phosphate (0, 25, and 100 ppm) (25 mL solution volume, 25 °C). After reaching equilibrium with either phosphate-containing or -free solutions, the final pHs had risen (Fig. 4b). The average final pH values were 9.4, 10.5, and 10.8 versus initial pH 2.2, 7, and 10 values, respectively. Surface deposited $Mg(OH)_2$, MgO, $Ca(OH)_2$, and $CaCO_3$ were identified on the CTL during XRD/XPS/EDX analysis. Ca^{2+} leaching from $CaCO_3$ dissolution in the CTL was negligible at pH 7 because of its lower solubility ($K_{sp} = 2.9 \times 10^{-9}$) versus $Ca(OH)_2$ ($K_{sp} = 5.5 \times 10^{-6}$). At pH 7, $Ca(OH)_2$ has a higher solubility than $Mg(OH)_2$ ($K_{sp} = 5.61 \times 10^{-12}$) (Table S2, supplementary information). This caused higher Ca^{2+} leaching (3.5 mg/L) than Mg^{2+} (2.6 mg/L) leaching in the absence of phosphates (Fig. 4c, d). These discharges were most pronounced at the initial pH 2.2. Dissolution of basic surface oxides/hydroxides ($Mg(OH)_2$, MgO, $CaCO_3$, and $Ca(OH)_2$) caused the equilibrium pH to rise. More dissolved Mg^{2+} and Ca^{2+} (15.2 ppm and 10 ppm) were detected when the initial solution pH = 2.2 than in solutions with an initial pH 7 (2.6 ppm and 3.5 ppm) or 10 (2.1 ppm and 2.9 ppm) in phosphate-free solutions (Fig. 4c, d). Of course, these pH values were time-dependent as pH changes with the adsorption of phosphate.

In the presence of the dissolved phosphates, pollutant species (speciation quantities which depend on the pH), $Mg_3(PO_4)_2$, $CaHPO_4$, $MgHPO_4$, and $Ca_3(PO_4)_2$ were deposited onto the CTL, as demonstrated by XRD/XPS analysis. When the phosphate concentration rose to 25 ppm, Ca^{2+} precipitates as less soluble $Ca_3(PO_4)_2$ ($K_{sp} = 2.1 \times 10^{-33}$), giving less measured Ca^{2+} leaching (2.2 mg/L) at pH 7 (Fig. 4d). Precipitated $Mg_3(PO_4)_2$ ($K_{sp} = 1.0 \times 10^{-24}$) from Mg^{2+} leaching is somewhat more soluble than $Ca_3(PO_4)_2$. Therefore, it leads to observing a slightly higher Mg^{2+} leaching amount (3.2 mg/L) than Ca^{2+} (Fig. 4c, d). Further increasing the phosphate concentration to 100 ppm released more Mg^{2+} (5.8 mg/L) from deposited $Mg_3(PO_4)_2$, whereas further dropping the amount of Ca^{2+} leaching (Fig. 4c, d). Reduced Mg^{2+} and Ca^{2+} leaching at pH 7 is attributed at least in part to the low CTL Langmuir adsorption capacity at pH 7 (see Section 3.4.3). Leaching of Mg^{2+} and Ca^{2+} from sorbents under acidic conditions was previously reported (Lim and Kim, 2017).

Partial dissolution of $Mg(OH)_2$, MgO, $Ca(OH)_2$, and $CaCO_3$ sites on the CTL surface is followed by precipitation of Ca^{2+} and Mg^{2+} phosphates/hydrophosphates and sorption occurs at protonated surfaces which attract HPO_4^{2-}/PO_4^{3-}. This gives high CTL P removal efficiency (19.9%) at pH = 2.2 (Fig. 4a). A control experiment conducted using acidic water (phosphate-free) at pH = 2.2, and 36% of the Mg and 72%

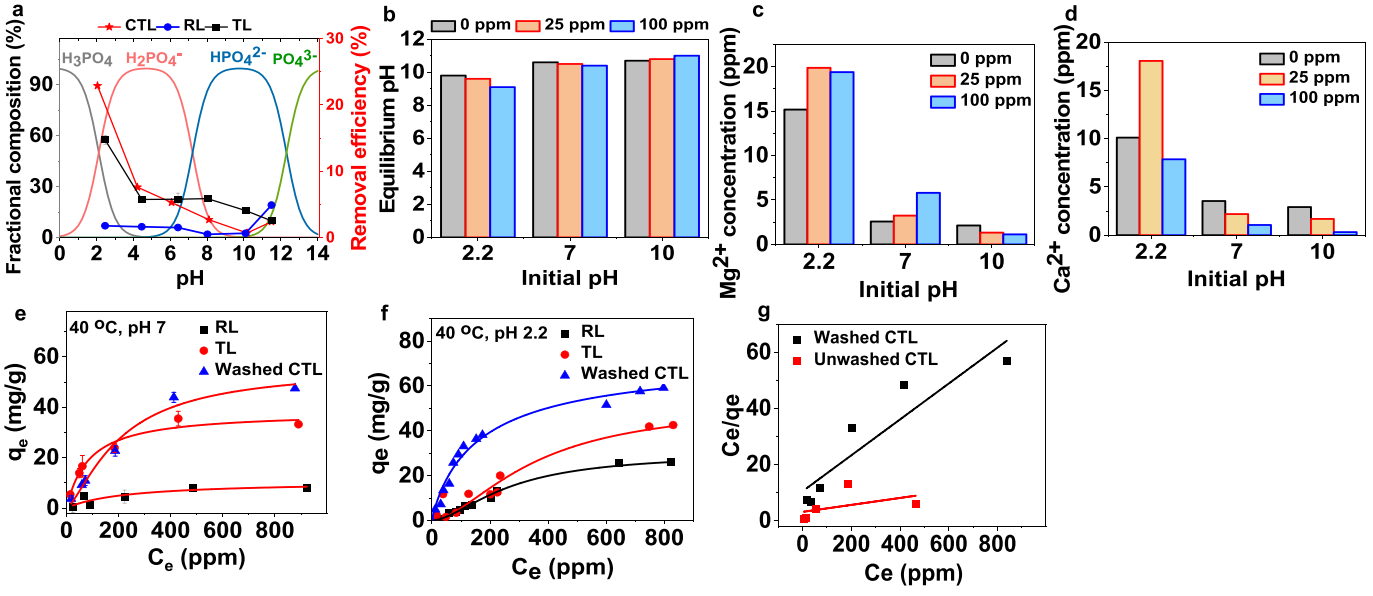

Fig. 4. a) Plots of RL, washed CTL, and TL phosphate removal efficiency (Right-Y axis) and phosphate's fractional composition (Left Y-axis) vs. pH at 25 °C (adsorbent dose 50 mg, 25 mL of 50 ppm [phosphate], 24 h, particle size 150–300 μm). b) Equilibrium pH vs. initial pH (2.2, 7, and 10) using washed CTL at 0, 25 and 100 ppm initial phosphate concentrations c) Leached Mg^{2+} concentration (ppm) and d) Ca^{2+} concentration (ppm) in the filtrates from initial solution pH values of 2.2, 7, and 10. Sips non-linear isotherms for RL, washed CTL and TL at e) 40 °C, pH 2.2, f) 40 °C, pH 7. g) Langmuir linear isotherms for washed CTL and unwashed CTL at 25 °C, pH 7 (adsorbent dose 50 mg, 25 mL of 25–1000 ppm phosphate concentration, 24 h).

of the Ca originally on CTL were leached into DI water. Therefore, precipitation-controlled P removal is also possible with CTL under an acidic pH. As the pH level increases, the CTL's P removal efficiency significantly decreased from 19.9% (pH = 2.2) to 0.3% (pH = 10). Several reasons govern this decline of P uptake. CTL's surface positive charge drops at high pH, which reduces the phosphate anion adsorption. High solution pH generates columbic repulsion between the deprotonated surface $Mg(OH)_2$/MgO sites and HPO_4^{2-}/PO_4^{3-}, lowering phosphate uptake. Lower amounts of Ca^{2+} and Mg^{2+} were released from CTL at high pH (Fig. 4c, d); therefore, phosphate precipitation declines. High Ca quantities can immobilize phosphate (Chen et al., 2007).

At low pH ~ 2, TL has greater phosphate adsorption than RL, due to the higher Al (0.9% vs 0.3%) and Mg contents (0.5% vs. 0.3%) (Table S1), and higher surface area (see Section 3.4). Al content on biochar improved phosphate adsorption (Yin et al., 2018). Lower surface area and a surface-cation-deficiency account for the lower P-binding of RL. A mild increase in RL adsorption at pH 11.5 may be caused by some surface OH groups ion exchanging with phosphate ions.

3.4.3. Adsorption isotherms and thermodynamics

Isotherm studies were conducted at the optimal pH (pH 2.2) and the environmentally relevant pH level (pH 7) (Fig. 4e, f). Washed CTL exhibited a higher maximum Sips P uptake capacity (74 mg/g) than RL (35 mg/g) and TL (50 mg/g) at 40 °C using 1000 ppm initial phosphate level (adsorbent dose 50 mg, 24 h, pH 2.2, particle size <150 μm) (Fig. 4e). Langmuir, Freundlich, and Sips isotherm model fitted parameters (Jeppu and Clement, 2012) are presented (Table S4–6). Regression coefficients were obtained for Langmuir (0.57–0.99), Freundlich (0.89–0.99), and Sips (0.98–1.00). The Sips model better describes phosphate removal by RL, TL, and washed CTL. All three of these phosphate removals are combined Langmuir-Freundlich processes, consistent with previous findings (Yao et al., 2013). The specific sorption per unit surface area of RL was greater (12.1 mg/m^2) than those of TL (0.4 mg/m^2) and washed CTL (1.2 mg/m^2) (40 °C, pH 2.2, particle size, particle size <150 μm). The BET surface areas of RL, TL, and CTL at the particle size <150 μm were 2.9 m^2/g, 120 m^2/g, and 60 m^2/g, respectively.

The isotherm studies were conducted for pyrolyzed and washed CTL, and pyrolyzed but unwashed CTL at pH 7, 25 °C (Fig. 4g). The washed CTL exhibited a maximum Langmuir phosphate removal capacity of 15.5 mg/g (Table 2) versus TL (2.5 mg/g) and RL (1.1 mg/g) (pH 7, particle size <150 μm, adsorbent dose 50 mg, 25 mL of 25–1000 ppm phosphate concentration, 24 h). Maximum Langmuir phosphate removal capacity of the unwashed CTL sample after pyrolysis at 600 °C (80.6 mg/g) (Table 2) was five times higher than that of washed CTL sample (15.5 mg/g) because far more $CaO/Ca(OH)_2$, $MgO/Mg(OH)_2$ and K_2CO_3 remained on the surface. The uptake capacities obtained at 25 °C and pH 7 (CTL, 15.5 mg/g, TL, 2.5 mg/g, and RL, 1.1 mg/g) are lower than the uptake capacities obtained at 25 °C, pH 2.2 (CTL, 24.8 mg/g, TL, 13.2 mg/g, and RL, 5.2 mg/g) (Table S6) due to the greater Ca^{2+}/Mg^{2+} dissolution from CTL at the more acidic pH which allows more HPO_4^{2-}/PO_4^{3-} to precipitate as Ca^{2+}/Mg^{2+} salts. Declining electrostatic attraction of HPO_4^{2-}/PO_4^{3-} with $MgO/Mg(OH)_2$ on CTL (PZC = 13) is also occurring at pH 7 compared to pH 2.2. Maximum phosphate sorption capacities of CTL (washed/unwashed) were compared with the previously developed adsorbents (Table 2).

Thermodynamic parameters (ΔG, ΔH, and ΔS) were calculated for all isothermal studies performed at pH 2.2 (Table S7). Phosphate sorption was spontaneous on RL, TL, and washed CTL (negative ΔG values) and all ΔH values were endothermic (positive). ΔH values were RL (308.9 kJ/mol) TL (241.5 kJ/mol), and washed CTL (100.4 kJ/mol) were consistent with chemisorption (greater than 40 kJ/mol) (Monárrez-Cordero et al., 2018) and not physisorption (less than 20 kJ/mol). This is consistent with the kinetic analysis. Positive values of ΔS (RL [1.11], TL [0.91], and washed CTL [0.43] kJ/mol) revealed increased randomness in the uptake processes.

3.5. Reuse, regeneration, and phosphate leaching by CTL

Washed and unwashed CTLs' recycling and use as a fertilizer was investigated after adsorbing phosphates. The phosphate adsorption-desorption was studied under 1000 ppm phosphate solution and 1.5 g of CTL dose, at pH 7, 25 °C (Fig. 5a, b). P-loaded CTL was desorbed with a 1 M NaOH stripping agent. Both the adsorption amount in each cycle (mg/g) and the cumulative amount of removed (mg/g) are presented. Washed CTL's P uptake decreased slightly more in the second cycle (98.3 mg/g) over the first cycle (108.0 mg/g) and decreased slightly in the third and fourth (94.7 and 90.0 mg/g) (Fig. 5a). About 113.0 mg/g of Phosphate adsorbed on unwashed CTL in the first cycle (Fig. 5b). This amount sharply dropped to (102.2, 98.9, and 94.7 mg/g) in the second, third and fourth cycles. However, only a very small fraction of the adsorbed or precipitated phosphates on both CTLs were desorbed in each cycle. While only these cycles were run, continued phosphate uptake would likely continue until no more Ca^{2+} or Mg^{2+} could leach from CTLs into the solution to precipitate phosphates. Stable $MgHPO_4$, $Mg_3(PO_4)_2$, $CaHPO_4$, and $Ca_3(PO_4)_2$ formation on CTLs and diffusion of phosphate moieties to CTLs pores may eventually cover leachable Ca^{2+} and Mg^{2+} oxides and hydroxides (Kajjumba et al., 2019). Desorption capacities were found by multiplying the equilibrium phosphate concentration by the stripping agent's volume and dividing it by the adsorbent weight. The P-laden washed CTL's desorption (mg/g) decreased each successive cycle (4.7 mg/g in cycle 1, 4.6 mg/g in cycle 2,

Table 2
Phosphate removal using different Mg and Ca-modified adsorbents.

Adsorbent	Initial (Mg/Ca compound: adsorbent) mass ratio	Experimental conditions	Adsorption capacity (mg/g)	Reference
Magnesium oxide nanoflake-modified diatomite adsorbent (MOD)	3:5 (as $MgCl_2 \cdot 6H_2O$)	PO_4^{3-} (100 mL), 4–50 mg/L, pH 5.0, MOD (50 mg), 12 h, 25 °C	45.7	(Xie et al., 2014)
Calcium decorated sludge carbon (Ca-SC)	2:1, 1:1 (as $CaCO_3$)	Adsorbent dosage 3 g/L. 200–1000 mg/L [Phosphate], 25 °C	116.8	(Kong et al., 2018)
Sugarcane bagasse biochar	1:1 ($MgCl_2 \cdot 6H_2O$ and $CaCl_2 \cdot 2H_2O$)	3–5800 mg/L [PO_4^{3-}], pH 2, 5, 10, 20, 40, 60, 80, 120, 240, 360, and 720 min, 25 °C	129.8	(Fang et al., 2020)
$Mg(OH)_2/ZrO_2$ composite (MZ)	6:5 ($MgCl_2 \cdot 6H_2O$ and $ZrOCl_2 \cdot 8H_2O$)	pH 7, 15 mg of adsorbent, 50 mL solution volume, 5 to 50 mg PO_4/L, 24 h, 25 °C	87.2 (PO_4)	(Lin et al., 2019)
Washed CTL	1:10 (as $MgSO_4$) 1:10 (as $CaSO_4$)	1–1000 ppm, 40 °C, pH 2.2, 25 mL solution volume, and 0.05 g of CTL	74	This study
Washed CTL	1:10 (as $MgSO_4$) 1:10 (as $CaSO_4$)	1–1000 ppm, 25 °C, pH 7, 25 mL solution volume, and 0.05 g of CTL	15.5	This study
Unwashed CTL	1:10 (as $MgSO_4$) 1:10 (as $CaSO_4$)	1–1000 ppm, 25 °C, pH 7, 25 mL solution volume, and 0.05 g of CTL	80.6	This study
Unwashed CTL	1:10 (as $MgSO_4$) 1:10 (as $CaSO_4$)	1–1000 ppm, 40 °C, pH 7, 25 mL solution volume, and 0.05 g of CTL	378.2	This study

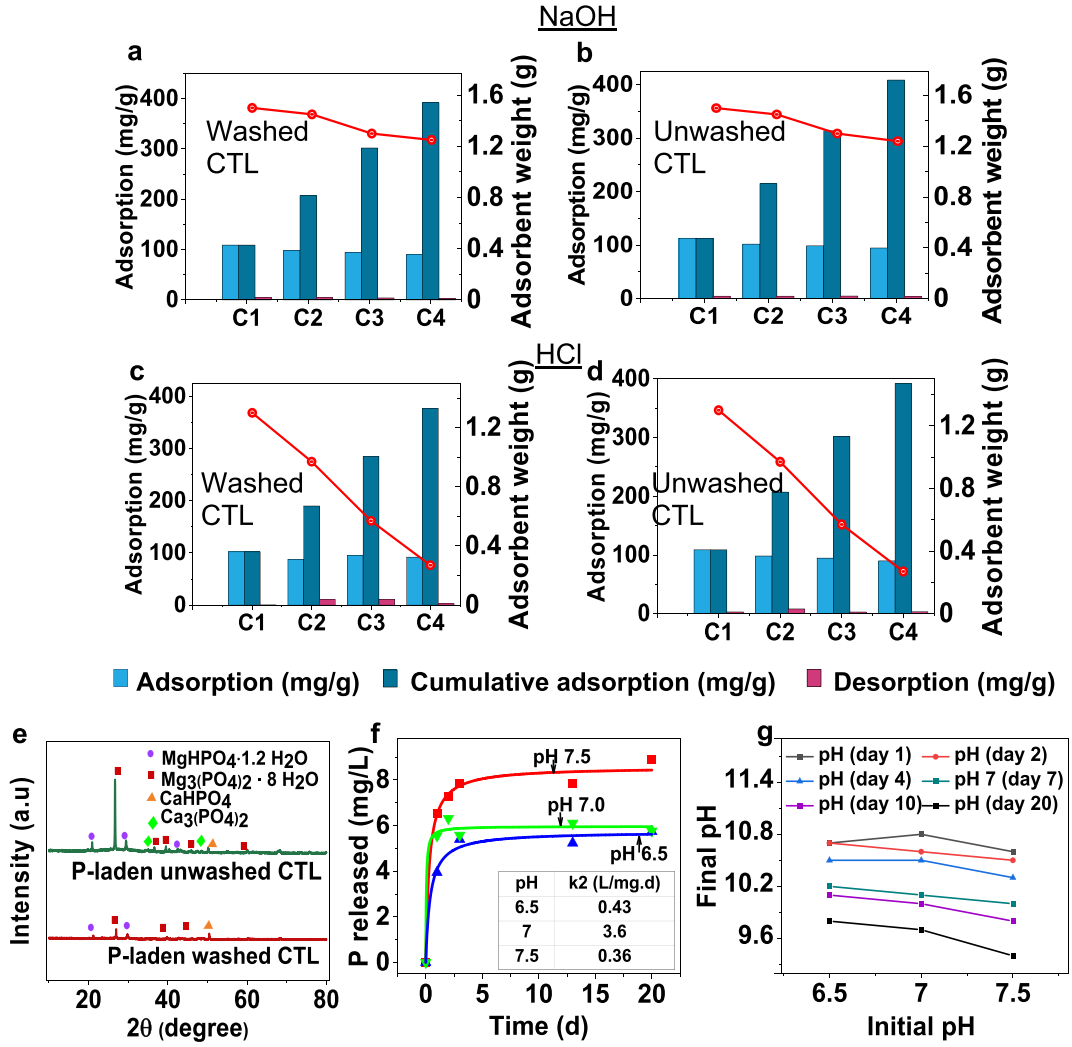

Fig. 5. a) Washed CTL and b) unwashed CTL adsorption-desorption tested for 4 cycles (adsorbent dose 50 mg, 25 mL of 1000 ppm phosphate, 24 h, pH 2.2, 40 °C). Desorption performed using 1 M NaOH as the stripping agent. c) Washed CTL and d) unwashed CTL adsorption-desorption test for 4 cycles, C1-C4 (adsorbent dose 1.5 g, 750 mL of 1000 ppm phosphate, 24 h, pH 7, 25 °C). Desorption performed using 0.5 M HCl (10 mL) as the stripping agent. Adsorbent weight (Right Y-axis) was lost after each cycle. e) XRD analysis of P-laden unwashed CTL and P laden washed CTL. f) phosphate desorption kinetics from washed CTL for 20 days. Equilibrium phosphate concentrations (Y-axis) were determined for pH 6.5, 7.0, and 7.5 DI water after 20 days (X-axis) (0.15 g of P-laden CTL where 17.3 mg of phosphate uptake occurred per g of CTL) was added into each pH level. f) Final pH after each day vs. initial pH of DI water.

4.2 mg/g in cycle 3, and 4.0 mg/g in cycle 4) slightly. 1 M NaOH is not a suitable phosphate stripper for phosphate because the precipitated Mg and Ca phosphates/hydrophosphates have very low solubilities in aqueous NaOH (Sugiyama et al., 2005). The inner-sphere complexation (ligand exchange) of surface R-OH (R = mineral or carbonaceous) sites for phosphate oxygen atoms to chemisorb as R-O-PO_3^{3-} (or its hydrogen phosphate analogs) is not the dominant mechanism of CTL's phosphate removal. Thus, basic stripping was unable to succeed in phosphate recovery (Wu et al., 2020). A 20 *w/v%* NaOH solution desorbed 80% phosphate from exhausted synthetic hydrocalcite, in which the reversible ion exchange is one of the major mechanisms (Kuzawa et al., 2006).

XRD patterns of P-laden unwashed CTL and washed CTL illustrate the crystallographic structures formed upon P uptake (Fig. 5e). In both spectra, calcium phosphates/hydrophosphates peak intensities are lower than the magnesium phosphates/hydrophosphates. This could be because $CaHPO_4$ (K_{sp}, 1.3×10^{-7}) is more highly soluble than $Mg_3(PO_4)_2$ (K_{sp}, 1.0×10^{-24}) (Table S2, supplementary materials) in aqueous solutions. This led to more Ca^{2+} in the solution than Mg^{2+} (Antunes et al., 2018). Stable $MgHPO_4$ and $Mg_3(PO_4)_2$ crystals are harder to desorb using 1 M NaOH. Very low (~3.8%) phosphate desorbability from $Mg(OH)_2$ abundant diatomite was reported in 1 mmol NaOH solution (Xie et al., 2014). A classic stripping process would need to efficiently dissolve the surface $Mg_3(PO_4)_2$, $CaHPO_4$, $MgHPO_4$ and $Ca_3(PO_4)_2$ salts deposited on CTL.

Batch desorptions were carried out by stirring the P-laden washed CTL and P-laden unwashed CTL with 10 mL of 0.5 M HCl. The amount desorbed by 0.5 M HCl from the washed CTL was 0 mg/g in the first cycle because phosphate precipitation as Ca^{2+}/Mg^{2+} salts is more preferable at acidic pH (Fig. 5c). The underlying Ca^{2+}/Mg^{2+} basic species leach into the solution, where they immediately reprecipitate as insoluble phosphates/hydrogen phosphates. More Ca^{2+}/Mg^{2+} leach from hydroxides, oxides, carbonates at pH 2.2, forming more phosphate and hydrophosphate salts precipitate back on the surface. Succeeding stripping cycles remove more phosphorus from the sorbent because less Ca^{2+}/Mg^{2+} species can strip from the dwindling supply of basic compounds on the surface. This causes the pH near the surface to drop and the water-insoluble phosphate and hydrogen phosphate precipitates can now dissolve in the acidic stripper solution near the surface. Phosphate adsorption onto washed CTL in the second cycle (87.6 mg/g) was lower than the first cycle (112.2 mg/g) because the sorbent active sites were mostly occupied by phosphates on the first cycle. Phosphates were desorbed (10.8 mg/g) in the second cycle (Fig. 5c), as the stronger acid (lower pH near the surface) could dissolve Mg and Ca phosphates/hydrophosphate. Each cycle might also dissolve some of

the Mg^{2+} and Ca^{2+} basic compounds originally deposited on washed CTL which might eventually deplete the original stoichiometric capability of washed CTL to precipitate insoluble phosphate salts on the CTL. Acidic desorption was employed by Li et al., 2016a and Zhang et al., 2019. Ca-bound P in earlier work was extracted using HCl (Mitrogiannis et al., 2017). Phosphate desorption from washed CTL decreased to 2 mg/g in the fourth cycle, without affecting the subsequent phosphate sorption performance. Desorptions (mg/g) obtained for washed CTL in HCl on two through four cycles (10.8 mg/g, 11.1 mg/g, and 2.5 mg/g) are higher than in NaOH on cycles 1–4 (4.7 mg/g, 4.6 mg/g, 4.2 mg/g, and 4.0 mg/g) (Fig. 5a, c). The adsorbent weight decreased after each cycle due to the dissolution of precipitated phosphate salts by HCl or weight loss caused by the filtering process after each cycle (Fig. 5c). This reduces the ability to use several adsorption/desorption cycles. This is not classic adsorption/desorption. These are stoichiometric dissolutions of $Ca(OH)_2$, $CaCO_3$, MgO, and $Mg(OH)_2$ with reprecipitation of $Mg_3(PO_4)_2$, $MgHPO_4$, $Ca_3(PO_4)_2$, and $CaHPO_4$, all occurring in competition as a function of the surrounding pH.

Phosphate uptake of unwashed CTL (108.8, 98.3, 96.7, and 92.0 mg/g) is far better than the washed CTL (102.2, 87.6, 94.9, and 90.0 mg/g) on four regeneration cycles (Fig. 5c, d). P-laden unwashed CTL has greater quantities of $Mg_3(PO_4)_2$, $MgHPO_4$, $Ca_3(PO_4)_2$, and $CaHPO_4$ than P-laden washed CTL (Fig. 5e), which can be attributed to its higher phosphate uptake. Furthermore, larger phosphate cumulative capacity was observed in unwashed CTL (391.8 mg/g) than washed CTL (374.7 mg/g) after four cycles. Therefore, exhausted unwashed CTL potentially improves soil fertility as it retained more phosphates. Higher desorption from P-laden unwashed CTL (3.1 mg/g) than from P-laden washed CTL (0 mg/g) was recorded in the first cycle. Low Ca/Mg phosphates/hydrophosphate quantities precipitated on P-laden washed CTL (Fig. 5b) could be more easily desorbed in HCl than unwashed CTL. The desorbed P from the exhausted washed CTL (~29,000 mg P kg^{-1}) and unwashed CTL (~19,100 mg P kg^{-1}) for 4 cycles are much higher than the level of soil P requirement, i.e., 45–50 mg P kg^{-1}.

Phosphate desorption kinetics of P-laden washed CTL was investigated at different pH levels (6.5, 7.0, and 7.5) using deionized water, and the data were fitted using a second-order kinetic model (Fig. 5f). Initially, phosphates were adsorbed onto the 0.45 g of the adsorbent used to follow desorption using 300 mL of 100 ppm PO_4^{3-} at pH 7. The phosphate uptake was 52 mg/g (under these conditions, washed CTL does not meet a saturation as the supply of solute concentration is inadequate for a large dose of the adsorbent). This P-laden material was divided equally into three portions and treated with different DI water (pH = 6.5, 7.0, and 7.5) solutions. The desorption of phosphates from these samples is shown in Fig. 5f. At all pH levels, the phosphate released rate is initially high before reaching equilibrium after 1–4 d (however, initial pH levels can be confusing since the pH became much more basic or contradict with the P-laden samples due to further basic Ca^{2+}/Mg^{2+} compounds remaining on their surfaces). Equilibrium released rates were 8 mg/L P at initial pH 7.5 ($t = 4$ d), 5.9 mg/L at initial pH 7 ($t = 2.5$ d), and 4 mg/L at initial pH 6.5 ($t = 1$ d). Therefore, washed CTL behaves as a slow-release fertilizer under different pH conditions. Slow-release fertilizers are beneficial because their nutrients are released slowly, avoiding the need for frequent soil applications.

At low pH, Ca/Mg phosphates tend to precipitate and becomes unavailable to plants. When the initial pH rose from pH 6.5 to 7.5, the equilibrium P concentrations in DI water also rose after 20 days where the final pH values were, 9.8, 9.7, and 9.4, respectively (Fig. 5f). The highest leached P concentration (8.9 mg/L) was found at pH = 7.5 after 20 d. The P adsorption affinity of washed CTL decreases as pH increases because the competition between phosphates and hydroxide ions is high. After day three, solutions with initial pH = 7 and 6.5 exhibited constant phosphate concentrations. After adding P-laden adsorbents, all solution pH values were initially greater than 10 before decreasing with time (Fig. 5g). P-loaded CTL (initial concentration, 100 ppm) underwent 52.9% (initial pH = 6.5), 51.7% (initial pH = 7), and 57.4% (initial pH = 7.5) PO_4^{3-} leaching within a 20-d period. Therefore, further studies are required to investigate the washed CTL's desorption behavior under optimum sorption conditions and utilize as a slow-release fertilizer for a relatively long period of time. The spent CTL adsorbent could replace current commercial P-based fertilizers to treat P deficient agricultural soils.

3.6. XPS analysis and CTL phosphate-binding interactions

Phosphate-binding interactions on CTL were further characterized by XPS before and after P removal. CTL high resolution (HR) C1s XPS spectrum before P uptake contained five deconvoluted peaks assigned to C-C/C-H (284.3 eV), C—O (285.2 eV), C═O (286.2 eV), COOR (287.1 eV), and CO_3^{2-} (290.0) (Table S9, Fig. 6a). After phosphate uptake, the atomic percentages of COOH and CO_3^{2-} on CTL dropped (from 1.3% to 0.7% and from 2.1% to 0.7%) (Table S9 and Fig. 6a, d). $CaCO_3$ dissolution at pH 2.2 explains the CO_3^{2-} atomic percentage reduction. The CTL HR O1s XPS spectrum was deconvoluted into five peaks belonging to metal hydroxides (M-OH) (530.0 eV), metal oxides (M-O) (531.0 eV), C—O (531.8 eV), C═O (532.7 eV), and COOR/ CO_3^{2-} (533.7 eV) (Table S10, Fig. 6b). CTL surface O percentages of C═O and CO_3^{2-} decreased from 17.9 to 10.2% and 12.8 to 7.7% after phosphate removal (Table S10). These oxygen content decrements imply the

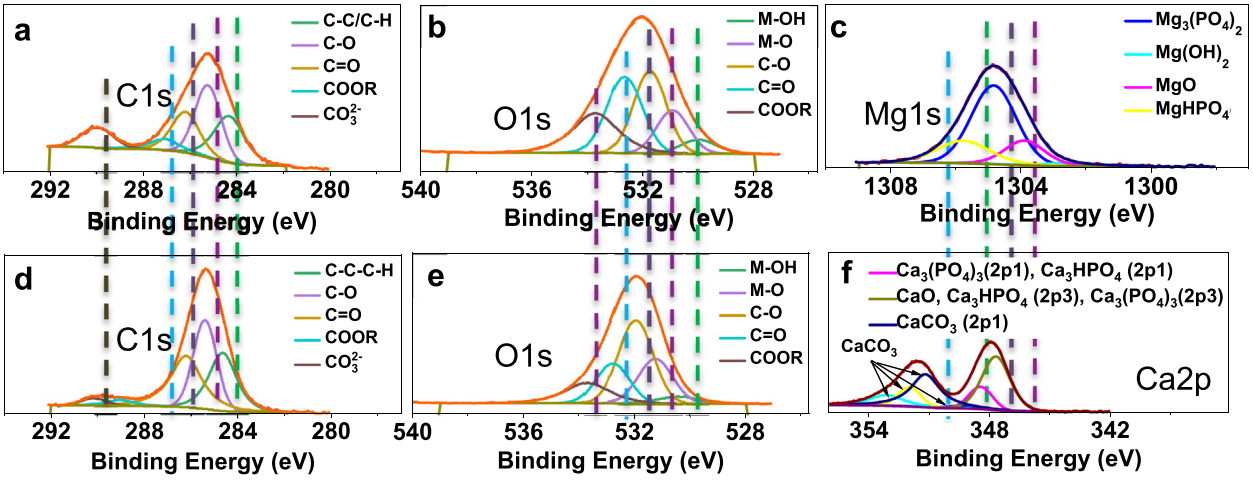

Fig. 6. XPS analysis of CTL before and after P removal. CTL HR C1s and O1S XPS spectra before (a, b) and after (d, e) P removal at pH 2.2. CTL HR Mg1s and Ca2p XPS spectra after (c, f) P removal at pH 2.2.

oxidation resistance of Mg—Ca impregnated biochar was enhanced, contributing to its soil stability as previously described (Wu et al., 2019).

After phosphate uptake at pH 2.2, the low-resolution CTL survey spectrum exhibited a new 134.9 eV peak due to surface phosphate precipitation (Fig. S5 and Table S8). The higher P atomic percentage of CTL (7.7%) versus RL (2.0%) and TL (4.3%) after phosphate uptake (Table S12) demonstrated CTL's greater phosphate sorption ability. There are two key processes involved in the phosphate uptake on Mg—Ca rich biochar; surface adsorption of phosphates (Li et al., 2016b; Yao et al., 2011) and $Mg(H_2PO_4)_2$, $MgHPO_4$, Ca $(H_2PO_4)_2$, and $CaHPO_4$ precipitation (Yao et al., 2013). However, the phosphate surface adsorption did not play a major role on CTL, as presented by SEM/EDX analysis. Precipitation dominated.

The P-laden CTL Mg1a spectrum had four key peaks at 1302.6 eV, 1303.9 eV, 1304.9 eV, and 1305.8 eV (Fig. 6c and Table S11), assigned respectively to $Mg(OH)_2$, MgO, $Mg_3(PO_4)_2$ and $MgHPO_4$ (Lin et al., 2019; Yao et al., 2013). This spectrum characterizes the surface Mg^{2+} deposition and crystalline Mg—P salts formation after P uptake. After CTL removes P at pH 2.2 from water, $Mg(OH)_2$ and MgO atomic percentages dropped from 2.0% to 0.2% and 3.6% to 1.0% (Fig. 6c), revealing dissolution of these species.

CTL has a very high PZC (~13), and both MgO and $Mg(OH)_2$ have PZCs around pH 12. When the solution pH is below the PZC, the adsorbent surface is positively charged; MgO, and CaO (if present) can acquire surface hydroxyls, whereas $Mg(OH)_2$ can be protonated (Yao et al., 2011). At low pH, HPO_4^{2-}/PO_4^{3-} electrostatically interact with protonated $Mg(OH)_2$ and MgO sites on CTL. Therefore, electrostatic interactions promote phosphate removal. Around pH ~ 4, P salts precipitate as $MgHPO_4$, $Mg_3(PO_4)_2$, and $CaHPO_4$. Lin et al., 2019 reported a similar Mg—P formation on the $Mg(OH)_2/ZrO_2$ surface during phosphate uptake.

After CTL's phosphate uptake, the M-OH surface region's oxygen percentage (for M = Al^{3+} or Si^{4+}) decreased (from 3.5% to 2.6%) (Table S10). The phosphate binding caused a drop of M-OH oxygen percentage on CTL, consistent with SEM/EDX studies. The ratio between M-OH of the adsorbent before phosphate exposure versus the P-laden adsorbent M-OH can be 0.5 (monodentate complex) or 2 (bidentate complex). Here, that ratio is 1.3 (3.5%/2.6%), which is within the permitted range. Mononuclear monodentate, mononuclear bidentate and binuclear bidentate phosphate complexes can potentially form Al and Si bound surface hydroxyls on CTL, in agreement with Lǔ findings (Lǔ et al., 2013). However, this inner sphere chemisorptive complexation is only a small fraction of the overall CTL phosphate uptake.

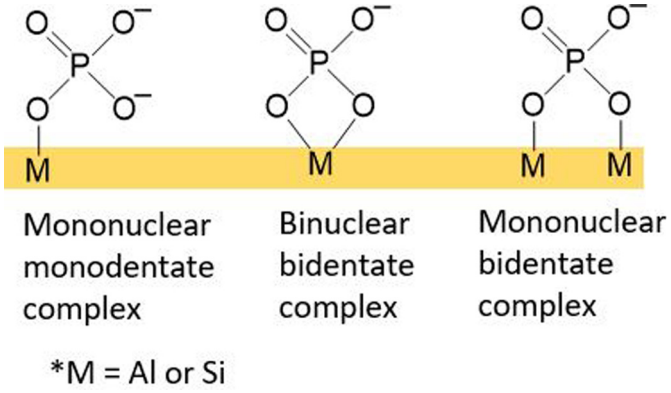

The HR-XPS Ca2p spectrum of P-laden CTL contains Ca2p3 peaks at 347.7 eV (CaO, $CaHPO_4$, $Ca_3(PO_4)_2$) and 348.5 eV ($Ca_3(PO_4)_2$, $CaHPO_4$), and a Ca2p1 peak at 349.5 eV ($CaCO_3$). This proves the existence of Ca^{2+} on the surface and possible Ca^{2+}/phosphate interactions (Fig. 6f and Table S11) (NIST, 2012). Bulk elemental analysis of CTL also indicated a 1.5% wt. Ca content. CO_2 is released on CTL pyrolysis of CTL and reacts with surface $Ca(OH)_2$, giving $CaCO_3$ (Antunes et al., 2018). XRD analysis of the CTL exhibited the known (112) plane of $CaCO_3$ at $2\theta = 29.7°$ (Fig. 1b). The atomic percentage of Ca in $CaCO_3$ decreased (from 1.3% to 0.3%) after phosphate uptake (Table S11) at pH 2.2. At low pH, dissolution of $CaCO_3$ followed by phosphate precipitation as $CaHPO_4$ caused this reduction. $CaCO_3$ is highly soluble in an acidic medium (Table S1), where it contributes more to phosphorous uptake via released Ca^{2+}. This Ca^{2+} formed brushite ($CaHPO_4$) or hydroxylapatite ($Ca_5(PO_4)_3OH$) precipitates (Antunes et al., 2018; Marshall et al., 2017). A new peak formation at 348.5 eV denotes $CaHPO_4$ (~1.5%) precipitation on the CTL.

Overall, CTL's Mg^{2+} and Ca^{2+} contents greatly exceeded RL's Mg (12.4% vs. 0.5%) and Ca (4.8% vs. 1.0%) (Table S11) and produced high phosphate uptake. After removing P from water, the P surface region percentage from XPS quantifications was highest in CTL (7.7%) vs TL and RL (4.3% vs. 2.0%) (Table S12 and Fig. S6). The HR P2p XPS spectrum's peaks were assigned to the 1.0% $MgHPO_4$ (132.9 eV), 4.5% $Mg_3(PO_4)_2$ (133.9 eV), and 2.2% $Ca_3(PO_4)_2$, $CaHPO_4$ (135.0 eV) (Table S12). Ca^{2+}or Mg^{2+}/HPO_4^{2-} complexes are thermodynamically more stable than $H_2PO_4^-$ (as discussed in Section 3.2) and interact with the positively charged adsorbent surfaces. Precipitation of $CaHPO_4$, $Ca_3(PO_4)_2$, $MgHPO_4$, and $Mg_3(PO_4)_2$ on the CTL surface increases surface P percentages as described above. In summary, CTL phosphate remediation proceeds largely via precipitation of Ca^{2+} and Mg^{2+} salts originally released by CTL (Eqs. (1)–(4)). At high pH (>9) speciation favors PO_4^{3-}, so $Ca_3(PO_4)_2$ was precipitated (Eq. (4)). The electrostatic interaction of protonated surfaces with HPO_4^{2-} and PO_4^{3-} species (Section 3.4.2) contributes CTL's P uptake under environmental pH levels (pH = 6–9).

$$Mg(OH)_2 + HPO_4^{2-} \rightarrow MgHPO_4 \quad (1)$$

$$3\,Mg(OH)_2 + 2PO_4^{3-} \rightarrow Mg_3(PO_4)_2 \quad (2)$$

$$Ca(OH)_2 + HPO_4^{2-} \rightarrow CaHPO_4 \quad (3)$$

$$3Ca(OH)_2 + 2PO_4^{3-} \rightarrow Ca_3(PO_4)_2 \quad (4)$$

4. Conclusions

Lignite-based adsorbents' high abundance, physico-chemical properties, and low-costs are attractive for traditional water treatment. These can be utilized to reduce eutrophication in natural waters by remediation of point and nonpoint sources of P. Sequential impregnation of lignite, RL, with Ca^{2+}/Mg^{2+} salts, followed by 600 °C pyrolysis (under N_2, for 1 h) generated CTL. The Sips P removal capacity at 25 °C of CTL (obtained after rinsing) was 15.5 mg/g versus TL and RL (2.5 and 1.1 mg/g) (particle size <150 μm, pH 7, adsorbent dose 50 mg, 25 mL of 25–1000 ppm phosphate concentration, 24 h). Enhanced CTL P removal capacity was due to increased surface availability of quantities of MgO, -$Mg(OH)_2$, -$Ca(OH)_2$, and -$CaCO_3$, which can dissolve into water and bind phosphate, or this plant nutrient can bind at the surface forming insoluble phosphate salts on the adsorbent. This stoichiometric process means P uptake capacities can be greatly expanded by greater Ca^{2+}/Mg^{2+} addition. CTL phosphate removal follows pseudo-second-order kinetics and precipitation dominates the phosphate removal by CTL. A variety of CTLs can be developed to remove phosphate fertilizers from agriculture run off and the spent sorbent can then be recycled as a slow-release fertilizer. Unwashed CTL could also be utilized to lower soil acidity, enhance soil fertility, and can be readily produced at a large scale in a few steps.

CRediT authorship contribution statement

Hasara Samaraweera: Writing- Original draft preparation, Investigation, Methodology, **Abigail Sharp:** Research support, **Charles U.**

Pittman Jr.: Supervision, Conceptualization, Writing - Review & Editing, **Xuefeng Zhang:** Research support, Review & Editing, **Rooban Venkatesh K G Thirumalai:** Data curation, Software, **El Barbary Hassan:** Data curation, resources, **Felio Perez:** Data curation, Software, **Sita Warren:** Supervision, **Claudia Reid:** Research support, **Todd Mlsna:** Conceptualization, Supervision, Project administration

Funding

This research did not receive any specific grant from funding agencies in the public, commercial, or not-for-profit sectors.

Declaration of competing interest

The authors declare that they have no known competing financial interests or personal relationships that could have appeared to influence the work reported in this paper.

Acknowledgements

Authors would like to acknowledge the Department of Chemistry, Mississippi State University financial support of this project. The authors also want to acknowledge North American Coal company, USA for donating lignite for the project. The authors additionally wish to thank the National Science Foundation INFEWS REU Program (Grant No. 1852527) for support of this work.

Appendix A. Supplementary data

Supplementary data to this article can be found online at https://doi.org/10.1016/j.scitotenv.2021.145631.

References

Antunes, E., Jacob, M.V., Brodie, G., Schneider, P.A., 2018. Isotherms, kinetics and mechanism analysis of phosphorus recovery from aqueous solution by calcium-rich biochar produced from biosolids via microwave pyrolysis. J. Environ. Chem. Eng. 6, 395–403. https://doi.org/10.1016/j.jece.2017.12.011.

Binitha, M.P., Pradyumnan, P.P., 2013. Dielectric Property Studies of Biologically Compatible Brushite Single Crystals Used as Bone Graft Substitute, 2013 https://doi.org/10.4236/jbnb.2013.42016.

Bombuwala Dewage, N., Liyanage, A.S., Mohan, D., Mlsna, T., Pittman Jr., C.U., 2018. Fast nitrate and fluoride adsorption and magnetic separation from water on α-Fe2O3 and Fe3O4 dispersed on Douglas fir biochar. Bioresour. Technol. 263, 258–265. https://doi.org/10.1016/j.biortech.2018.05.001.

Bowen, B.H., Irwin, M.W., 2008. Coal Characteristics.

Buscarino, G., Ardizzone, V., Vaccaro, G., Gelardi, F.M., 2011. Sintering process of amorphous SiO2 nanoparticles investigated by AFM, IR and Raman techniques. J. Non-Cryst. Solids, SiO2. Advanced Dielectrics and Related Devices 357, 1866–1870. https://doi.org/10.1016/j.jnoncrysol.2010.11.114.

Cao, X., Harris, W., 2010. Properties of dairy-manure-derived biochar pertinent to its potential use in remediation. Bioresour. Technol. 101, 5222–5228. https://doi.org/10.1016/j.biortech.2010.02.052.

Carvalho, L., McDonald, C., de Hoyos, C., Mischke, U., Phillips, G., Borics, G., Poikane, S., Skjelbred, B., Solheim, A.L., Wichelen, J.V., Cardoso, A.C., 2013. Sustaining recreational quality of European lakes: minimizing the health risks from algal blooms through phosphorus control. J. Appl. Ecol. 50, 315–323. https://doi.org/10.1111/1365-2664.12059.

Chen, J., Kong, H., Wu, D., Chen, X., Zhang, D., Sun, Z., 2007. Phosphate immobilization from aqueous solution by fly ashes in relation to their composition. J. Hazard. Mater. 139, 293–300. https://doi.org/10.1016/j.jhazmat.2006.06.034.

Chen, S.S., Cao, Y., Tsang, D.C.W., Tessonnier, J.-P., Shang, J., Hou, D., Shen, Z., Zhang, S., Ok, Y.S., Wu, K.C.-W., 2020. Effective dispersion of MgO nanostructure on biochar support as a basic catalyst for glucose isomerization. ACS Sustain. Chem. Eng. 8, 6990–7001. https://doi.org/10.1021/acssuschemeng.0c00278.

Criado, Y.A., Alonso, M., Abanades, J.C., 2014. Kinetics of the CaO/Ca(OH)2 hydration/dehydration reaction for thermochemical energy storage applications. Ind. Eng. Chem. Res. 53, 12594–12601. https://doi.org/10.1021/ie404246p.

Dodds, W.K., Bouska, W.W., Eitzmann, J.L., Pilger, T.J., Pitts, K.L., Riley, A.J., Schloesser, J.T., Thornbrugh, D.J., 2009. Eutrophication of U.S. freshwaters: analysis of potential economic damages. Environ. Sci. Technol. 43, 12–19. https://doi.org/10.1021/es801217q.

Du, W., Li, Y., Xu, X., Shang, Y., Gao, B., Yue, Q., 2019. Selective removal of phosphate by dual Zr and La hydroxide/cellulose-based bio-composites. J. Colloid Interface Sci. 533, 692–699. https://doi.org/10.1016/j.jcis.2018.09.002.

Dung, N.T., Unluer, C., 2017. Carbonated MgO concrete with improved performance: the influence of temperature and hydration agent on hydration, carbonation and strength gain. Cem. Concr. Compos. 82, 152–164. https://doi.org/10.1016/j.cemconcomp.2017.06.006.

Egle, L., Rechberger, H., Krampe, J., Zessner, M., 2016. Phosphorus recovery from municipal wastewater: an integrated comparative technological, environmental and economic assessment of P recovery technologies. Sci. Total Environ. 571, 522–542. https://doi.org/10.1016/j.scitotenv.2016.07.019.

Fang, C., Zhang, T., Li, P., Jiang, R., Wu, S., Nie, H., Wang, Y., 2015. Phosphorus recovery from biogas fermentation liquid by Ca–Mg loaded biochar. J. Environ. Sci. 29, 106–114. https://doi.org/10.1016/j.jes.2014.08.019.

Fang, L., Li, J., Donatello, S., Cheeseman, C.R., Poon, C.S., Tsang, D.C.W., 2020. Use of Mg/Ca modified biochars to take up phosphorus from acid-extract of incinerated sewage sludge ash (ISSA) for fertilizer application. J. Clean. Prod. 244, 118853. https://doi.org/10.1016/j.jclepro.2019.118853.

Fraissard, J.P., Conner, C.W., 1997. Physical Adsorption: Experiment, Theory, and Applications (Springer Science & Business Media).

Hasson, D., Shemer, H., Semiat, R., 2016. Removal of scale-forming ions by a novel cation-exchange electrochemical system—a review. Desalination Water Treat. 57, 23147–23161. https://doi.org/10.1080/19443994.2015.1098806.

Huang, W., Zhang, Y., Li, D., 2017. Adsorptive removal of phosphate from water using mesoporous materials: a review. J. Environ. Manag. 193, 470–482. https://doi.org/10.1016/j.jenvman.2017.02.030.

Hung, I.-M., Shih, W.-J., Hon, M.-H., Wang, M.-C., 2012. The properties of sintered calcium phosphate with [Ca]/[P] = 1.50. Int. J. Mol. Sci. 13, 13569–13586. https://doi.org/10.3390/ijms131013569.

Inagaki, M., 2006. Carbon Materials Science and Engineering: From Fundamentals to Applications. 清华大学出版社有限公司.

Jeppu, G.P., Clement, T.P., 2012. A modified Langmuir-Freundlich isotherm model for simulating pH-dependent adsorption effects. J. Contam. Hydrol. Sorption and Transport Processes Affecting the Fate of Environmental Pollutants in the Subsurface 129–130, 46–53. https://doi.org/10.1016/j.jconhyd.2011.12.001.

de Jonge, H., Mittelmeijer-Hazeleger, M.C., 1996. Response to Comment on "Adsorption of CO2 and N2 on Soil Organic Matter: Nature of Porosity, Surface Area, and Diffusion Mechanisms." Environ. Sci. Technol. 30, 3636–3637. doi:https://doi.org/10.1021/es962011r.

Kajjumba, G.W., Yıldırım, E., Aydın, S., Emik, S., Ağun, T., Osra, F., Wasswa, J., 2019. A facile polymerisation of magnetic coal to enhanced phosphate removal from solution. J. Environ. Manag. 247, 356–362. https://doi.org/10.1016/j.jenvman.2019.06.088.

Karthikeyan, M., Zhonghua, W., Mujumdar, A.S., 2009. Low-rank coal drying technologies—current status and new developments. Dry. Technol. 27, 403–415. https://doi.org/10.1080/07373930802683005.

Karunanayake, A.G., Navarathna, C.M., Gunatilake, S.R., Crowley, M., Anderson, R., Mohan, D., Perez, F., Pittman Jr., C.U., Mlsna, T., 2019. Fe3O4 nanoparticles dispersed on Douglas fir biochar for phosphate sorption. ACS Appl. Nano Mater. 2, 3467–3479. https://doi.org/10.1021/acsanm.9b00430.

Kong, L., Han, M., Shih, K., Su, M., Diao, Z., Long, J., Chen, D., Hou, L., Peng, Y., 2018. Nanorod Ca-decorated sludge derived carbon for removal of phosphorus. Environ. Pollut. 233, 698–705. https://doi.org/10.1016/j.envpol.2017.10.099.

Kuzawa, K., Jung, Y.-J., Kiso, Y., Yamada, T., Nagai, M., Lee, T.-G., 2006. Phosphate removal and recovery with a synthetic hydrotalcite as an adsorbent. Chemosphere 62, 45–52. https://doi.org/10.1016/j.chemosphere.2005.04.015.

Langer, M., Väänänen, J., Boulestreau, M., Miehe, U., Bourdon, C., Lesjean, B., 2017. Advanced phosphorus removal via coagulation, flocculation and microsieve filtration in tertiary treatment. Water Sci. Technol. J. Int. Assoc. Water Pollut. Res. 75, 2875–2882. https://doi.org/10.2166/wst.2017.166.

Leo, C.P., Chai, W.K., Mohammad, A.W., Qi, Y., Hoedley, A.F.A., Chai, S.P., 2011. Phosphorus removal using nanofiltration membranes. Water Sci. Technol. 64, 199–205. https://doi.org/10.2166/wst.2011.598.

Li, R., Wang, J.J., Zhou, B., Awasthi, M.K., Ali, A., Zhang, Z., Gaston, L.A., Lahori, A.H., Mahar, A., 2016a. Enhancing phosphate adsorption by Mg/Al layered double hydroxide functionalized biochar with different Mg/Al ratios. Sci. Total Environ. 559, 121–129. https://doi.org/10.1016/j.scitotenv.2016.03.151.

Li, R., Wang, J.J., Zhou, B., Awasthi, M.K., Ali, A., Zhang, Z., Lahori, A.H., Mahar, A., 2016b. Recovery of phosphate from aqueous solution by magnesium oxide decorated magnetic biochar and its potential as phosphate-based fertilizer substitute. Bioresour. Technol. Waste Biorefinery - Advocating Circular Economy 215, 209–214. https://doi.org/10.1016/j.biortech.2016.02.125.

Lim, B.H., Kim, D.-J., 2017. Selective acidic elution of Ca from sewage sludge ash for phosphorus recovery under pH control. J. Ind. Eng. Chem. 46, 62–67. https://doi.org/10.1016/j.jiec.2016.10.016.

Lin, J., He, S., Wang, X., Zhang, H., Zhan, Y., 2019. Removal of phosphate from aqueous solution by a novel mg(OH)2/ZrO2 composite: adsorption behavior and mechanism. Colloids Surf. Physicochem. Eng. Asp. 561, 301–314. https://doi.org/10.1016/j.colsurfa.2018.11.001.

Lozano-Calero, D., Martìn-Palomeque, P., Madueño-Loriguillo, S., 1996. Determination of phosphorus in cola drinks. J. Chem. Educ. 73, 1173. https://doi.org/10.1021/ed073p1173.

Lǐ, J., Liu, H., Liu, R., Zhao, X., Sun, L., Qu, J., 2013. Adsorptive removal of phosphate by a nanostructured Fe–Al–Mn trimetal oxide adsorbent. Powder Technol. 233, 146–154. https://doi.org/10.1016/j.powtec.2012.08.024.

Marshall, J.A., Morton, B.J., Muhlack, R., Chittleborough, D., Kwong, C.W., 2017. Recovery of phosphate from calcium-containing aqueous solution resulting from biochar-induced calcium phosphate precipitation. J. Clean. Prod. 165, 27–35. https://doi.org/10.1016/j.jclepro.2017.07.042.

Mastronardo, E., Bonaccorsi, L., Kato, Y., Piperopoulos, E., Lanza, M., Milone, C., 2016. Thermochemical performance of carbon nanotubes based hybrid materials for MgO/H2O/

Mg(OH)2 chemical heat pumps. Appl. Energy 181, 232–243. https://doi.org/10.1016/j.apenergy.2016.08.041.
McLaughlin, H., 2012. Analytical Options for Biochar Adsorption and Surface Area 15.
Milicevic, S., Boljanac, T., Martinovic, S., Vlahovic, M., Milosevic, V., Babic, B., 2012. Removal of copper from aqueous solutions by low cost adsorbent-Kolubara lignite. Fuel Process. Technol. 95, 1–7. https://doi.org/10.1016/j.fuproc.2011.11.005.
Mitrogiannis, D., Psychoyou, M., Baziotis, I., Inglezakis, V.J., Koukouzas, N., Tsoukalas, N., Palles, D., Kamitsos, E., Oikonomou, G., Markou, G., 2017. Removal of phosphate from aqueous solutions by adsorption onto Ca(OH)2 treated natural clinoptilolite. Chem. Eng. J. 320, 510–522. https://doi.org/10.1016/j.cej.2017.03.063.
Mohan, D., Pittman Jr., C.U., 2006. Activated carbons and low cost adsorbents for remediation of tri- and hexavalent chromium from water. J. Hazard. Mater. 137, 762–811. https://doi.org/10.1016/j.jhazmat.2006.06.060.
Monárrez-Cordero, B.E., Sáenz-Trevizo, A., Bautista-Carrillo, L.M., Silva-Vidaurri, L.G., Miki-Yoshida, M., Amézaga-Madrid, P., 2018. Simultaneous and fast removal of As3+, As5+, Cd2+, Cu2+, Pb2+ and F− from water with composite Fe-Ti oxides nanoparticles. J. Alloys Compd. 757, 150–160. https://doi.org/10.1016/j.jallcom.2018.05.013.
Mosa, A., El-Ghamry, A., Tolba, M., 2020. Biochar-supported natural zeolite composite for recovery and reuse of aqueous phosphate and humate: batch sorption–desorption and bioassay investigations. Environ. Technol. Innov. 19, 100807. https://doi.org/10.1016/j.eti.2020.100807.
Navarathna, C.M., Bombuwala Dewage, N., Keeton, C., Pennisson, J., Henderson, R., Lashley, B., Zhang, X., Hassan, E.B., Perez, F., Mohan, D., Mlsna, T., Pittman Jr., C.U., 2020. Biochar adsorbents with enhanced hydrophobicity for oil spill removal. ACS Appl. Mater. Interfaces 12, 9248–9260. https://doi.org/10.1021/acsami.9b20924.
NIST, 2012. NIST XPS Database Detail Page [WWW Document]. URL https://srdata.nist.gov/xps/XPSDetailPage.aspx?AllDataNo=66523 (accessed 3.28.19).
Nixon, S.W., 2012. Coastal marine eutrophication: a definition, social causes, and future concerns. Ophelia. https://doi.org/10.1080/00785236.1995.10422044.
Pehlivan, E., Arslan, G., 2007. Removal of metal ions using lignite in aqueous solution—low cost biosorbents. Fuel Process. Technol. 88, 99–106. https://doi.org/10.1016/j.fuproc.2006.09.004.
Qi, Y., Hoadley, A.F.A., Chaffee, A.L., Garnier, G., 2011. Characterisation of lignite as an industrial adsorbent. Fuel 90, 1567–1574. https://doi.org/10.1016/j.fuel.2011.01.015.
Quartz R100134 - RRUFF Database [WWW Document], 2020. URL https://rruff.info/Quartz/R100134 (accessed 10.30.20).
Scheidema, M.N., Taskinen, P., 2011. Decomposition thermodynamics of magnesium sulfate. Ind. Eng. Chem. Res. 50, 9550–9556. https://doi.org/10.1021/ie102554f.
Simate, G.S., Maledi, N., Ochieng, A., Ndlovu, S., Zhang, J., Walubita, L.F., 2016. Coal-based adsorbents for water and wastewater treatment. J. Environ. Chem. Eng. 4, 2291–2312. https://doi.org/10.1016/j.jece.2016.03.051.
Sugiyama, S., Yokoyama, M., Ishizuka, H., Sotowa, K.-I., Tomida, T., Shigemoto, N., 2005. Removal of aqueous ammonium with magnesium phosphates obtained from the ammonium-elimination of magnesium ammonium phosphate. J. Colloid Interface Sci. 292, 133–138. https://doi.org/10.1016/j.jcis.2005.05.073.
Takaya, C.A., Fletcher, L.A., Singh, S., Okwuosa, U.C., Ross, A.B., 2016. Recovery of phosphate with chemically modified biochars. J. Environ. Chem. Eng. 4, 1156–1165. https://doi.org/10.1016/j.jece.2016.01.011.
US EPA, O., 2015. National Recommended Water Quality Criteria - Aquatic Life Criteria Table [WWW Document]. US EPA. URL https://www.epa.gov/wqc/national-recommended-water-quality-criteria-aquatic-life-criteria-table (accessed 9.20.20).
US EPA, O., 2018. Nutrient Criteria Technical Guidance Manuals [WWW Document]. US EPA. URL https://www.epa.gov/nutrient-policy-data/nutrient-criteria-technical-guidance-manuals (accessed 12.4.20).
Wu, L., Wei, C., Zhang, S., Wang, Y., Kuzyakov, Y., Ding, X., 2019. MgO-modified biochar increases phosphate retention and rice yields in saline-alkaline soil. J. Clean. Prod. 235, 901–909. https://doi.org/10.1016/j.jclepro.2019.07.043.
Wu, B., Wan, J., Zhang, Y., Pan, B., Lo, I.M.C., 2020. Selective phosphate removal from water and wastewater using sorption: process fundamentals and removal mechanisms. Environ. Sci. Technol. 54, 50–66. https://doi.org/10.1021/acs.est.9b05569.
Wuthier, R.E., Rice, G.S., Wallace, J.E., Weaver, R.L., LeGeros, R.Z., Eanes, E.D., 1985. In vitro precipitation of calcium phosphate under intracellular conditions: formation of brushite from an amorphous precursor in the absence of ATP. Calcif. Tissue Int. 37, 401–410. https://doi.org/10.1007/BF02553710.
Xie, F., Wu, F., Liu, G., Mu, Y., Feng, C., Wang, H., Giesy, J.P., 2014. Removal of phosphate from eutrophic lakes through adsorption by in situ formation of magnesium hydroxide from diatomite. Environ. Sci. Technol. 48, 582–590. https://doi.org/10.1021/es4037379.
Yang, Q., Wang, X., Luo, W., Sun, J., Xu, Q., Chen, F., Zhao, J., Wang, S., Yao, F., Wang, D., Li, X., Zeng, G., 2018. Effectiveness and mechanisms of phosphate adsorption on iron-modified biochars derived from waste activated sludge. Bioresour. Technol. 247, 537–544. https://doi.org/10.1016/j.biortech.2017.09.136.
Yao, Y., Gao, B., Inyang, M., Zimmerman, A.R., Cao, X., Pullammanappallil, P., Yang, L., 2011. Removal of phosphate from aqueous solution by biochar derived from anaerobically digested sugar beet tailings. J. Hazard. Mater. 190, 501–507. https://doi.org/10.1016/j.jhazmat.2011.03.083.
Yao, Y., Gao, B., Chen, J., Yang, L., 2013. Engineered biochar reclaiming phosphate from aqueous solutions: mechanisms and potential application as a slow-release fertilizer. Environ. Sci. Technol. 47, 8700–8708. https://doi.org/10.1021/es4012977.
Yin, Q., Zhang, B., Wang, R., Zhao, Z., 2017. Biochar as an adsorbent for inorganic nitrogen and phosphorus removal from water: a review. Environ. Sci. Pollut. Res. 24, 26297–26309. https://doi.org/10.1007/s11356-017-0338-y.
Yin, Q., Ren, H., Wang, R., Zhao, Z., 2018. Evaluation of nitrate and phosphate adsorption on Al-modified biochar: influence of Al content. Sci. Total Environ. 631–632, 895–903. https://doi.org/10.1016/j.scitotenv.2018.03.091.
Zanchett, G., Oliveira-Filho, E.C., 2013. Cyanobacteria and cyanotoxins: from impacts on aquatic ecosystems and human health to anticarcinogenic effects. Toxins 5, 1896–1917. https://doi.org/10.3390/toxins5101896.
Zhang, R., Wang, B., Ma, H., 2010. Studies on chromium (VI) adsorption on sulfonated lignite. Desalination 255, 61–66. https://doi.org/10.1016/j.desal.2010.01.016.
Zhang, M., Gao, B., Yao, Y., Xue, Y., Inyang, M., 2012. Synthesis of porous MgO-biochar nanocomposites for removal of phosphate and nitrate from aqueous solutions. Chem. Eng. J. 210, 26–32. https://doi.org/10.1016/j.cej.2012.08.052.
Zhang, M., Gao, B., Yao, Y., Inyang, M., 2013. Phosphate removal ability of biochar/MgAl-LDH ultra-fine composites prepared by liquid-phase deposition. Chemosphere 92, 1042–1047. https://doi.org/10.1016/j.chemosphere.2013.02.050.
Zhang, Q., Zhang, Z., Teng, J., Huang, H., Peng, Q., Jiao, T., Hou, L., Li, B., 2015. Highly efficient phosphate sequestration in aqueous solutions using nanomagnesium hydroxide modified polystyrene materials. Ind. Eng. Chem. Res. 54, 2940–2949. https://doi.org/10.1021/ie503943z.
Zhang, Y., Guo, X., Yao, Y., Wu, F., Zhang, C., Lu, J., 2016. Synthesis of mg-decorated carbon nanocomposites from MesoCarbon MicroBeads (MCMB) graphite: application for wastewater treatment. ACS Omega 1, 417–423. https://doi.org/10.1021/acsomega.6b00073.
Zhang, J., Hu, X., Zhang, K., Xue, Y., 2019. Desorption of calcium-rich crayfish shell biochar for the removal of lead from aqueous solutions. J. Colloid Interface Sci. 554, 417–423. https://doi.org/10.1016/j.jcis.2019.06.096.
Zhao, L., Guanhua, N., Hui, W., Qian, S., Gang, W., Bingyou, J., Chao, Z., 2020. Molecular structure characterization of lignite treated with ionic liquid via FTIR and XRD spectroscopy. Fuel 272, 117705. https://doi.org/10.1016/j.fuel.2020.117705.
Zhong, C., Deng, Y., Hu, W., Qiao, J., Zhang, L., Zhang, J., 2015. A review of electrolyte materials and compositions for electrochemical supercapacitors. Chem. Soc. Rev. 44, 7484–7539. https://doi.org/10.1039/C5CS00303B.
Zhou, H., Jiang, Z., Wei, S., 2013. A novel absorbent of nano-Fe loaded biomass char and its enhanced adsorption capacity for phosphate in water [WWW document]. J. Chem. https://doi.org/10.1155/2013/649868.